Homonuclear Zero-Quantum Recoupling in Fast Magic-Angle Spinning Nuclear Magnetic Resonance

Andreas Brinkmann,*,[1] Jörn Schmedt auf der Günne,*,[2] and Malcolm H. Levitt*,†,[3]

*Division of Physical Chemistry, Arrhenius Laboratory, Stockholm University, 10691 Stockholm, Sweden; and
†Department of Chemistry, Southampton University, Southampton S017 1BJ, United Kingdom

Solid-state magic-angle-spinning NMR pulse sequences which implement zero-quantum homonuclear dipolar recoupling are designed with the assistance of symmetry theory. The pulse sequences are compensated on a short time scale by the use of composite pulses and on a longer time scale by the use of supercycles. ^{13}C dipolar recoupling is demonstrated in powdered organic solids at high spinning frequencies. The new sequences are compared to existing pulse sequences by means of numerical simulations. Experimental two-dimensional magnetization exchange spectra are shown for [U-^{13}C]-L-tyrosine. © 2002 Elsevier Science (USA)

1. INTRODUCTION

Solid-State NMR, especially when combined with isotopic labeling, is capable of extracting molecular structural information and may be applied to systems which are unsuitable for diffraction or solution NMR. Methods exist for the determination of internuclear distances (*1–21*) and molecular torsional angles (*22–30*). These methods have been applied to noncrystalline biological macromolecules (*31, 32*) providing otherwise inaccessible information.

In many realistic applications it is necessary to use magic-angle spinning (MAS) to achieve sufficient sensitivity and resolution. Molecular structural information is obtained by applying radio frequency (rf) pulse sequences, in order to selectively recouple the anisotropic spin interactions which are suppressed by the magic-angle spinning. A particular important class of pulse sequences restores the magnetic dipole–dipole interactions between spins of the same isotopic type. Such *homonuclear dipolar recoupling* methods make accessible proximity, distance, and angular information under high-resolution conditions. Homonuclear dipole–dipole recoupling methods may be classified in terms of the rotational symmetry of the recoupled spin Hamiltonian around the main magnetic field. Double-quantum

recoupling sequences have been extensively developed and applied (*13–19*). Zero-quantum recoupling sequences have also proved to be useful, particularly for obtaining two-dimensional longitudinal magnetization exchange spectra which indicate the qualitative spatial proximity of spin sites (*33–39*).

An ideal zero-quantum recoupling sequence should have the following characteristics: (i) The magnitude of the recoupled dipole–dipole interaction should be as large as possible; (ii) the sequence should be feasible at high spinning frequencies, in order to ensure good resolution and to minimize spinning sidebands generated by chemical shift anisotropy (CSA) interactions during signal acquisition; (iii) the sequence should have a minimal dependence on isotropic and anisotropic chemical shifts; (iv) the rf field requirement should be low. The latter condition is particularly important in organic solids where a simultaneous decoupling field must often be applied at the ^{1}H resonance frequency.

A number of zero-quantum recoupling methods exist, but so far none meets all of these requirements. For example, rotational resonance (*1–3*) does not need an rf field but is very narrowband since it relies on isotropic chemical shift differences. DRAMA (*8*) is sensitive to isotropic and anisotropic chemical shifts. DRAWS (*10*) is more broadband but has high rf field requirements and cannot realistically be implemented at high spinning frequencies. In addition, DRAWS does not generate a pure zero-quantum average Hamiltonian. RIL (*11, 12, 40*) and USEME (*41*) work very well at low spinning frequencies, but are also difficult to implement at high spinning frequencies because of rf field limitations.

The most widely used zero-quantum recoupling sequence is probably the radio-frequency driven recoupling (RFDR) sequence, which consists of a train of π pulses separated in time by the sample rotation period (*42–44*). The performance of RFDR in the presence of finite rf fields and general π pulses has been analyzed recently (*45*). In this form, the pulse sequence is known as finite-pulse RFDR (fpRFDR) (*45*).

We have recently shown how pulse sequence design in solid-state MAS NMR is facilitated by the use of symmetry principles (*14, 18, 20, 21, 46–49*). These principles allow the recoupling and decoupling properties of a wide range of pulse sequences to

---

[1] Present address: Physical Chemistry/Solid State NMR, University of Nijmegen, Toernooiveld 1, 6525 ED Nijmegen, The Netherlands.

[2] Present address: Department of Inorganic Chemistry, University of Bonn, Gerhard-Domagk-Straße 1, 53121 Bonn, Germany.

[3] To whom correspondence should be addressed. E-mail: Malcolm.Levitt@soton.ac.uk.

be assessed, at least to a first approximation, by evaluating a set of simple integer inequalities. The results of these inequalities may be deduced by a diagrammatic technique without detailed calculation. In addition, it is possible to identify sets of pulse sequence symmetries that lead to the recoupling properties of interest. The symmetry theory may be applied to two broad pulse sequence classes, denoted in general CN_n^ν and RN_n^ν. The integers N, n and ν are called the symmetry numbers of the pulse sequence. The meaning of these symbols is explained below.

In this paper we apply the symmetry principles to the problem of deriving a homonuclear zero-quantum recoupling sequence. We derive a set of pulse sequence symmetries which implement selective zero-quantum recoupling in first order average Hamiltonian theory. Candidate pulse sequences are constructed by choosing an appropriate basic element and supercycling procedure. The pulse sequence performance is judged by simulated magnetization exchange curves of $^{13}C_2$ spin systems in labeled glycine, alanine, and serine. Field dependent calculations for these three substances are presented in order to compare the new sequences with the RIL and fpRFDR sequences. We demonstrate the new pulse sequences by two-dimensional correlation experiments on [U-^{13}C]-L-tyrosine, at spinning frequencies of 15.000 and 23.000 kHz.

2. THEORY

2.1. RN_n^ν Sequences

The RN_n^ν sequences and their theory have been introduced in Refs. 18 and 48. Here we briefly review the main results.

2.1.1. Construction principles. RN_n^ν sequences are defined on the basis of the space-spin symmetry of the interaction frame Hamiltonian terms (18, 48). One possible implementation of the RN_n^ν sequences employs a basic pulse sequence element, denoted $\mathcal{R}$, of duration $n\tau_r/N$, where $\tau_r = 2\pi/\omega_r$ is the spinning period (ω_r is the angular spinning frequency). n, ν, and N are integer symmetry numbers. N is constrained to be even. The element $\mathcal{R}$ rotates the spins by an odd multiple of π around the x axis in the rotating frame, if all interactions other than that with the rf field are ignored. For example $\mathcal{R}$ could be a simple 180° pulse around the x axis ($\mathcal{R} = 180_0$). We use the standard notation for rectangular rf pulses: ξ_ϕ, where ξ is the flip angle (nutation frequency multiplied by the pulse duration) and ϕ is the rf phase, taking into account the sign of the gyromagnetic ratio (50, 51). In this paper, the flip angles and the phases are written in degrees. The basic element $\mathcal{R}$ may also be a composite 180° pulse or some other modulated rf field scheme. It is also possible to use basic elements containing windows, in which the rf field is turned off for some time.

A second basic element, denoted $\mathcal{R}'$, is derived from $\mathcal{R}$ by changing the sign of all rf phases. The RN_n^ν sequence is composed of $N/2$ $(\mathcal{R})_\phi(\mathcal{R}')_{-\phi}$ pairs, where the additional phase shift is given by $\phi = \pi\nu/N$, and ν is the third symmetry number of

the pulse sequence. The duration of the whole RN_n^ν sequence is given by $n\tau_r$. In many cases, the complete RN_n^ν sequences are repeated many times, sometimes with supercycle variations (see below).

2.1.2. Space-spin selection rules. Consider a spin system experiencing internal spin interactions as well as a rotor-synchronized rf pulse sequence with the symmetry RN_n^ν. As described before (46, 48), the first order result for the effective Hamiltonian is

$$\bar{H}^{(1)} = \sum_{\Lambda,l,m,\lambda,\mu} \bar{H}_{lm\lambda\mu}, \qquad [1]$$

where the symbol Λ represents the type of interaction (chemical shift, spin–spin coupling), and the quantum numbers l, m, λ, μ index the symmetry of the term with respect to rotations of the spin polarizations and with respect to spatial rotations of the sample. The term $\bar{H}_{lm\lambda\mu}^\Lambda(t)$ transforms as an irreducible spherical tensor of rank l for spatial rotations and rank λ for spin rotations. The component indices m and μ have values $m = -l, -l+1, \ldots, l$ for space and $\mu = -\lambda, -\lambda+1, \ldots, \lambda$ for spin. If rf irradiation is applied to only one channel, the direct dipole–dipole coupling between homonuclear spin pairs has ranks $l = 2$, $\lambda = 2$; the J-coupling between homonuclear spin pairs has ranks $l = 0$, $\lambda = 0$; the isotropic chemical shift has ranks $l = 0$, $\lambda = 1$; the chemical shift anisotropy and heteronuclear dipolar couplings have ranks $l = 2$, $\lambda = 1$. All components with $l = 2$, $m = 0$ vanish in the case of exact magic-angle spinning.

As shown in Refs. 46 and 48, the RN_n^ν symmetry leads to the following symmetry theorem for the first order average Hamiltonian

$$\bar{H}_{lm\lambda\mu}^\Lambda = 0 \quad \text{if} \quad mn - \mu\nu \neq \frac{N}{2}Z_\lambda, \qquad [2]$$

where Z_λ is an integer with the same parity as λ (i. e., if $\lambda =$ even, then $Z_\lambda = 0, \pm 2, \pm 4, \ldots$; if $\lambda =$ odd, then $Z_\lambda = \pm 1, \pm 3, \pm 5, \ldots$). Similar theorems exist for the higher order Magnus terms (18, 46, 48). The result Eq. [2] allows the design of sequences with desirable recoupling properties without considering the detailed structure of the basic element $\mathcal{R}$, at least in the first stage of the calculation.

The magnitudes of the symmetry allowed terms depend on the pulse sequence. In general, a symmetry-allowed term in the first order effective Hamiltonian has the form

$$\bar{H}_{lm\lambda\mu}^\Lambda = \omega_{lm\lambda\mu} T_{\lambda\mu}^\Lambda, \qquad [3]$$

where

$$\omega_{lm\lambda\mu} = \kappa_{lm\lambda\mu}\left[A_{lm}^\Lambda\right]^R \exp\left\{-im\left(\alpha_{RL}^0 - \omega_r t_0^0\right)\right\}. \qquad [4]$$

Here $[A_{lm}^\Lambda]^R$ is a space component of the interaction tensor Λ, written in the rotor-fixed frame, α_{RL}^0 denotes the initial rotor

position and t_0^0 is the initial time point of the pulse sequence. $[A_{lm}^{\Lambda}]^R$ is obtained in the rotor-fixed frame by transforming it from the principal axis system as follows:

$$\left[A_{lm}^{\Lambda}\right]^R = \sum_{m'',m'} \left[A_{lm''}^{\Lambda}\right]^P D_{m''m'}^l\left(\Omega_{PM}^{\Lambda}\right) D_{m'm}^l(\Omega_{MR}). \quad [5]$$

The Euler angles $\Omega_{PM}^{\Lambda} = \{\alpha_{PM}^{\Lambda}, \beta_{PM}^{\Lambda}, \gamma_{PM}^{\Lambda}\}$ describe the relative orientation of the principal axis frame of the interaction Λ and a molecule-fixed frame, and depend on the molecular and electronic structure. The Euler angles $\Omega_{MR} = \{\alpha_{MR}, \beta_{MR}, \gamma_{MR}\}$ relate the molecular frame to a frame fixed on the rotor, and are random variables in a powder.

The definition of the scaling factor $\kappa_{lm\lambda\mu}$ and a calculation procedure for general basic elements $\mathcal{R}$ are given in Ref. 48.

2.2. Homonuclear Zero-Quantum Recoupling

2.2.1. Pulse sequence symmetries. The selection rule Eq. [2] may be used to design zero-quantum homonuclear recoupling sequences, which provide a time-independent average Hamiltonian of the form

$$\bar{H}^{(1)} = \sum_{j<k} \bar{H}_{jk}^{(1)}, \quad [6]$$

where

$$\bar{H}_{jk}^{(1)} = \omega_{jk}\frac{1}{\sqrt{6}}\left(2S_{jz}S_{kz} - \frac{1}{2}(S_j^- S_k^+ + S_j^+ S_k^-)\right) + 2\pi J_{jk}\mathbf{S}_j\cdot\mathbf{S}_k.$$
$$[7]$$

The sum is taken over all homonuclear spin-pairs, J_{jk} is the J-coupling between spins S_j and S_k and ω_{jk} is the recoupled through-space dipolar interaction, which is a real number. The exact form of ω_{jk} depends on the recoupling sequence chosen and will be discussed later. The homonuclear J-coupling has symmetry numbers $(l, m, \lambda, \mu) = (0, 0, 0, 0)$ and is therefore symmetry-allowed under any $\text{C}N_n^{\nu}$ and $\text{R}N_n^{\nu}$ sequence.

Table 1 shows some $\text{R}N_n^{\nu}$ symmetries suitable for homonuclear zero-quantum recoupling. All sequences recouple the homonuclear dipolar coupling terms with quantum numbers $(l, m, \lambda, \mu) = \{(2, 1, 2, 0),\ (2, -1, 2, 0),\ (2, 2, 2, 0),\ (2, -2, 2, 0)\}$ in the first order average Hamiltonian. At the same time, all other homonuclear dipolar interactions, all chemical shift anisotropies, all isotropic chemical shifts, and all heteronuclear couplings are suppressed.

The operation of the symmetry $\text{R}6_6^2$ is explained in Fig. 1 with the help of a space-spin selection diagram (SSS diagram) (47). The levels in Fig. 1 indicate the total value of $mn - \mu\nu$, broken into two stages, so as to separate the effects of spatial rotations and spin rotations. The barriers at the right-hand side of both diagrams have holes separated by N units. The position of the holes is determined by the parity of λ, which corresponds to the

TABLE 1
Inequivalent RN_n^{ν} Symmetries for Homonuclear Zero-Quantum Recoupling, with Suppression of All Chemical Shift Anisotropies, Isotropic Chemical Shifts, and Heteronuclear Couplings

N	n	ν	N	n	ν	N	n	ν
4	4	1	4	12	1	4	16	1
6	6	1	6	12	1	8	16	1
6	6	2	6	12	2	8	16	3
4	8	1	12	12	1	16	16	1
8	8	1	12	12	5	16	16	3
8	8	3	14	14	1	16	16	5
10	10	1	14	14	2	16	16	7
10	10	2	14	14	3	6	18	1
10	10	3	14	14	4	18	18	1
10	10	4	14	14	5	18	18	2
			14	14	6	18	18	4
						18	18	5
						18	18	7
						18	18	8

Note. In all cases, the symmetry-allowed terms are given by $(l, m, \lambda, \mu) = \{(2, 2, 2, 0),\ (2, -2, 2, 0),\ (2, 1, 2, 0),\ (2, -1, 2, 0)\}$ (homonuclear dipole–dipole coupling terms) and $(0, 0, 0, 0)$ (homonuclear isotropic J-couplings). Sequences with $N \leq 18$, $n \leq 18$ and $0 \leq \nu \leq N/2$ are shown. Additional variants with identical first order selection rules are given by $\text{R}N_n^{ZN\pm\nu}$ where Z is an integer.

inequality in the symmetry theorem Eq. [2]. Figure 1a shows the case of chemical shift anisotropy. In this case, λ is odd, so the position of each hole corresponds to an odd multiple of $N/2$, i.e., $\pm 3, \pm 9, \ldots$. For the homonuclear dipolar couplings in Fig. 1b, on the other hand, λ is even, so the position of each hole corresponds to an even multiple of $N/2$, i.e., $0, \pm 6, \pm 12, \ldots$. Figure 1a shows that the symmetry $\text{R}6_6^2$ suppresses all CSA components ($m = \{\pm 1, \pm 2\}$ and $\mu = \{0, \pm 1\}$) in the first order average Hamiltonian. Figure 1b shows that only homonuclear dipolar components with $(m, \mu) = \{(1, 0), (2, 0)\}$ are symmetry allowed (and by implication also $(m, \mu) = \{(-1, 0), (-2, 0)\}$). All components of the isotropic chemical shift ($m = 0$ and $\mu = \{0, \pm 1\}$) are also suppressed (diagram not shown). The fact that the $\mu = 0$ term is associated with several spatial components leads to a recoupled dipolar Hamiltonian, that is *not* γ-encoded. As a result, the total amplitude ω_{jk} of the recoupled homonuclear zero-quantum Hamiltonian depends on the angle γ_{MR}. The lack of γ-encoding leads to attenuated dipolar oscillations in a powder sample (see below). However, in the applications explored in this paper, this disadvantage is outweighed by the greater freedom for supercycle construction made available by the lack of gamma-encoding. The extended supercycle stabilizes the performance of the sequence over long time scales. Our experience suggests that the case for and against gamma-encoding may depend on the time scale and the type of application: In the case of quantitative experiments over short timescales, gamma-encoded sequences may be preferable, while for qualitative correlations over long timescales, supercycled non-gamma-encoded sequences may be easier to implement reliably.
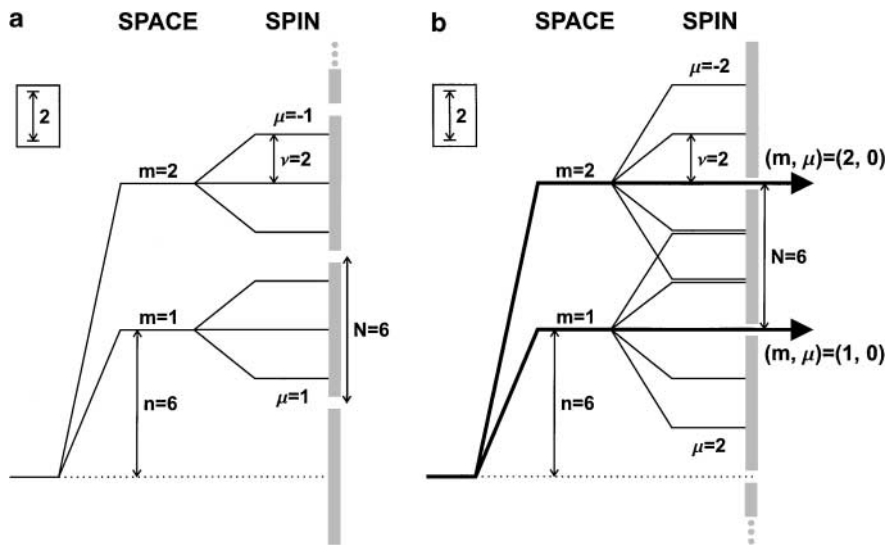
FIG. 1. Space-spin selection diagram for the $R6_6^2$ sequence: (a) suppression of all CSA components; (b) selection of two ZQ dipole–dipole components, with quantum numbers $(m, \mu) = (1, 0)$ and $(2, 0)$. The mirror image pathways stemming from $m = -1$, $m = -2$ have been suppressed for simplicity.

The symmetry $R4_4^1$ is of particular interest. In this case, the phase $\pi \nu / N$ is given by $\pi/4 = 45°$. If the basic element $\mathcal{R}$ consists of a strong π_x-pulse in the middle of an interval of length τ_r, one obtains the RFDR sequence with the XY-4 phase cycle (52) for the π-pulses. This symmetry goes some way towards explaining the success of this phase cycle.

Recently, Ishii suggested generalized RFDR sequences, referred to as finite pulse rf driven recoupling sequences (fpRFDR), based on general π pulse elements (45), which have overall phases given by $\phi_l = \{1 + (-1)^l\}\pi/L$, where $L \geq 4$ is an even integer and $l = 1, \ldots, L$. These suggested sequences correspond to our solutions of the type RN_N^1, with $N = L$, e.g., $R4_4^1$, $R6_6^1$, $R8_8^1$, $R10_{10}^1$, ... Note however that Table 1 contains many solutions that do not conform to this definition, for example $R6_6^2$, $R8_8^3$, $R10_{10}^2$, $R10_{10}^3$, and $R10_{10}^4$.

Although the symmetry relationships simplify the construction of rf pulse sequences and lead rapidly to usable solutions, it is conceivable that good solutions also exist outside the framework of the symmetry theory. See Ref. 53 for further discussion of the uses and limitations of symmetry-based pulse sequence design in MAS NMR.

2.2.2. Scaling factors. For the sequences in Table 1, the term ω_{jk} in Eq. [7] is given by

$$\omega_{jk} = \sum_{m=1}^{2} \left(\omega_{2m20}^{jk} + \omega_{2-m20}^{jk} \right) \qquad [8]$$

$$= 2 \operatorname{Re}\left(\sum_{m=1}^{2} \omega_{2m20}^{jk} \right), \qquad [9]$$

where the recoupled through-space homonuclear dipolar interactions ω_{2m20}^{jk} for $m = 1, 2$ are given by Eq. [4]. They depend

on the molecular orientation and the starting time point of the recoupling sequence t_0^0

$$\omega_{2m20}^{jk}(\Omega_{MR}, t_0^0) = \sqrt{6}\, b_{jk} \kappa_{2m20} e^{im(\omega_r t_0^0 - \alpha_{RL}^0 - \gamma_{MR})}$$

$$\times \sum_{m'=-2}^{2} d_{0m'}^{(2)}(\beta_{PM}^{jk}) d_{m'm}^{(2)}(\beta_{MR}) e^{-im'(\gamma_{PM}^{jk} + \alpha_{MR})}, \qquad [10]$$

where the Euler angles $\Omega_{PM}^{jk} = \{\alpha_{PM}^{jk} \beta_{PM}^{jk} \gamma_{PM}^{jk}\}$ describe the transformation of each homonuclear dipole–dipole coupling from its principal axis system to a molecule fixed frame. The through-space dipolar coupling constant between two spins j and k is given by

$$b_{jk} = -\frac{\mu_0}{4\pi} \frac{\gamma^2 \hbar}{r_{jk}^3}, \qquad [11]$$

where r_{jk} is the spin–spin internuclear distance.

The terms κ_{2m20} in Eq. [10] are the scaling factors of the recoupled dipolar interaction terms. These scaling factors depend on the basic element $\mathcal{R}$ and may be calculated using the procedure presented in Ref. 48. The scaling factors for a selection of pulse sequences are listed in Table 2. The first row corresponds to a RFDR sequence (42–44) in the limit of infinitely strong 180° pulses ($\tau_p = 0$). Both scaling factors disappear in this case. This implies that RFDR sequences using strong pulses do not lead to recoupling of the homonuclear dipolar couplings in first order average Hamiltonian theory. The second row in Table 2 refers to a fpRFDR sequence (45) in which the 180° pulse has a finite duration. In this case the two scaling factors are small but finite, with a strong dependence on the ratio of the pulse length τ_p and the rotor period τ_r.

TABLE 2
The Scaling Factors κ_{2m20} for a Selection of RN_n^ν Sequences

Symmetry	$\mathcal{R}$	$|\omega_{nut}^{max}/\omega_r|$	κ_{2120}	κ_{2220}	Remark
$R4_4^1$	$\tau_r/2\text{–}180_0\text{–}\tau_r/2$	∞	0	0	$\tau_p = 0$
$R4_4^1$	$19\tau_r/20\text{–}180_0\text{–}19\tau_r/20$	5.0	0.043	-0.030	$\tau_p = \tau_r/10$
$R4_4^1$	$90_{180}270_0$	1.0	0	0.153	
$R4_4^1$	$90_{270}90_090_{90}90_090_{90}270_090_0$	1.5	0	0.152	
$R6_6^2$	$90_{180}270_0$	1.0	0	0.153	
$R6_6^2$	$90_{270}90_090_{90}90_090_{90}270_090_0$	1.5	0	0.152	

Note. The ratio of the peak rf nutation frequency to the spinning frequency is also given. The first row corresponds to RFDR with a XY-4 phase cycle. The second row corresponds to fpRFDR with $L = 4$, using the specified relationship between the π pulse duration τ_p and the spinning period τ_r.

The above analysis assumes that the spin interaction terms are expressed in the interaction frame of the rf field alone. If the isotropic chemical shifts are also included in the interaction frame, then the recoupled dipolar interaction does appear in the first order average Hamiltonian, even for infinitely strong rf pulses (*42–44, 54*). In the treatment given here, the dipolar recoupling for strong pulse RFDR only appears in the second order cross terms between chemical shifts and dipolar couplings. It should be possible to extend the symmetry theory to encompass more complicated interaction frames, although this approach often encounters technical difficulties associated with the lack of cyclicity of the interaction frame over the pulse sequence period.

The scaling factors of finite-pulse RFDR with simple 180_0 pulses are small. We have explored the use of other basic elements, and some results are also given in Table 2.

For the basic elements $\mathcal{R} = 90_{180}270_0$ and $\mathcal{R} = 90_{270}90_0 90_{90}90_090_{270}90_0$, the scaling factors κ_{2120} disappear and the scaling factors κ_{2220} are reasonable large real numbers. In general, the scaling factors for the symmetries in Table 1 are real numbers if the elements $\mathcal{R}$ are amplitude modulated (i.e., they contain phase shifts which are integer multiples of $180°$).

2.3. Supercycles

Numerical simulations show that the pulse sequences based on the symmetries in Table 1 alone are not satisfactorily robust with respect to isotropic chemical shifts and chemical shift anisotropies. We have therefore employed supercycles in order to improve the robustness of the zero-quantum recoupling sequences.

One possible supercycle is created by concatenating an RN_n^ν sequence with a $RN_n^{-\nu}$ sequence. In the general case, the $RN_n^{-\nu}$ sequence is obtained from the RN_n^ν sequence by reversing the sign of *all* rf phases, including any internal phases within the $\mathcal{R}$ elements. The resulting supercycled sequence is denoted $RN_n^\nu RN_n^{-\nu}$.

In Ref. *47* we calculated the relationships between the first and second order average Hamiltonians for the case of a

CN_n^ν sequence and the corresponding $CN_n^{-\nu}$ sequence. These results may be directly applied to the case of complete RN_n^ν sequences.

As shown in Ref. *47*, the concatenation of RN_n^ν and $RN_n^{-\nu}$ sequences destroys the γ-encoding of the average Hamiltonian. However, in the case of the zero-quantum homonuclear recoupling sequences in Table 1, the first order average Hamiltonian is not γ-encoded from the beginning. In the case of a γ-dependent zero-quantum average Hamiltonian of the type Eq. [7] the supercycled $RN_n^\nu RN_n^{-\nu}$ sequence generates the same first order average Hamiltonian as the basic RN_n^ν sequence.

In addition to the selection rules for the second order terms in the average Hamiltonian, presented in Refs. *18* and *48*, the supercycle $RN_n^\nu RN_n^{-\nu}$ suppresses the second order term $\bar{H}_{l_2m_2\lambda_2\mu_2;l_1m_1\lambda_1\mu_1}^{l_2 \times l_1}$ if $\lambda_1 = \lambda_2$ and $\mu_1 + \mu_2 = 0$. For example, the symmetry $R6_6^2$ allows 32 CSA × CSA cross terms between different components of the same CSA tensor. All these cross terms are suppressed for the supercycle $R6_6^2 R6_6^{-2}$.

The $RN_n^\nu RN_n^{-\nu}$ supercycle also stabilizes the pulse sequence against rf phase shift errors, which are a serious problem for many RN_n^ν sequences (*19*).

Figure 2 shows numerically exact two-spin simulations of longitudinal magnetization transfer between the CO and C^α sites in $^{13}C_2$-glycine at a field of $B_0 = 9.4$ T and a spinning frequency of $\omega_r/2\pi = 38.500$ kHz. A number of supercycled $R6_6^2$ zero-quantum recoupling sequences with the basic element $\mathcal{R} = 90_{180}270_0$ are compared. The spin interaction parameters are given in the caption of Fig. 6. The longitudinal magnetization transferred from the CO to the C^α site is plotted as a function of the mixing interval τ_{mix}. All curves rise rapidly at short mixing times and oscillate at long mixing times. The oscillation frequency depends on the recoupled dipolar interaction and the isotropic J-coupling.

The solid line in Fig. 2a corresponds to the case in which only the homonuclear direct dipolar coupling is included. The J-coupling, the isotropic and anisotropic chemical shifts are ignored. This curve therefore corresponds to "ideal" zero-quantum recoupling. The dashed lines correspond to simulations including both isotropic and anisotropic chemical shifts for $R6_6^2$ sequences with and without supercycles.

As may be seen, the simple $R6_6^2$ sequence is poorly compensated for isotropic chemical shifts and CSA. The improvement in performance by the $R6_6^2 R6_6^{-2}$ supercycle is significant, underlining the importance of the CSA × CSA cross terms in degrading the poor performance of the simple $R6_6^2$ sequence in realistic circumstances.

The performance of the $RN_n^\nu RN_n^{-\nu}$ supercycle is improved further by repeating the entire sequence, with an additional overall phase shift, incremented in three steps

$$\left[RN_n^\nu RN_n^{-\nu}\right]_0 \left[RN_n^\nu RN_n^{-\nu}\right]_{120} \left[RN_n^\nu RN_n^{-\nu}\right]_{240}, \quad [12]$$

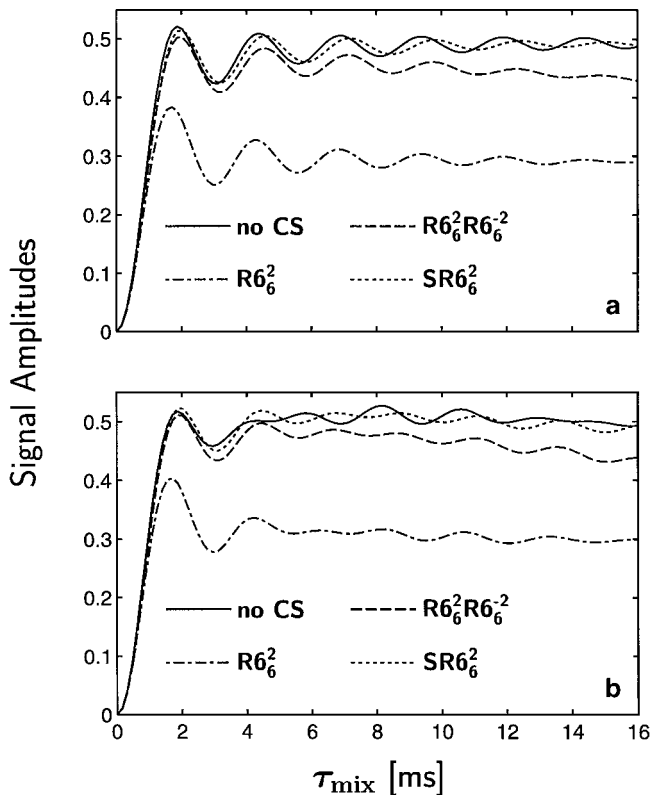where the notation $[\ldots]_\phi$ indicates an overall phase shift of the

FIG. 2. Simulated transferred longitudinal magnetization from the CO to the C^α sites for different supercycles of $R6_6^2$ with the basic element $\mathscr{R} = 90_{180}270_0$. The simulations use the parameters of $^{13}C_2$-glycine, given in the caption of Fig. 6, at a field of $B_0 = 9.4$ T and spinning frequency of $\omega_r/2\pi = 38.500$ kHz: (a) simulations without the J-coupling; (b) simulations with the J-coupling; (solid lines) simulations of the basic $R6_6^2$ sequence without chemical shifts; (dashed lines) simulations including both isotropic and anisotropic chemical shifts, using the basic $R6_6^2$ sequence, the $R6_6^2R6_6^{-2}$ and the $SR6_6^2$ supercycle in Eq. [14]. Powder averaging was performed using 6044 molecular orientations, chosen according to the ZCW scheme (79).

bracketed sequence by ϕ. This supercycle removes residual (±1) and (±2)-quantum terms in the average Hamiltonian.

As may be seen in Fig. 2a, this supercycle provides the highest amplitude of exchanged longitudinal magnetization at long mixing times. The oscillations of the transferred magnetization are also relatively unperturbed, as compared to the modulations in the absence of chemical shifts.

The RFDR sequence with the XY-8 phase cycle (52) corresponds to the supercycle $R4_4^1R4_4^{-1}$. The RFDR sequence with the XY-16 phase cycle (52) corresponds to the supercycle $[R4_4^1R4_4^{-1}]_0[R4_4^1R4_4^{-1}]_{180}$. We tried this supercycle together with the $R6_6^2$ sequence, but obtained slightly worse performance than with the supercycle given in Eq. [12].

The simulations in Fig. 2b include a 53.1 Hz homonuclear J-coupling in addition to the other interactions. As may be seen, the J-coupling tends to obscure the recoupled dipolar oscillations, but the qualitative performance of the sequence is unchanged.

2.4. Sequence Selection

In order to identify good sequences, we selected a variety of composite pulse elements $\mathscr{R}$ which are known to be robust from experience in other fields (55).

The scaling factor of the recoupled interaction depends on the choice of the basic element $\mathscr{R}$. Generally speaking, it is desirable to choose the basic element so as to maximize at least one of the two scaling factors κ_{2120} and κ_{2220}.

As a first step, we calculated the scaling factors κ_{2120} and κ_{2220}, demanding a absolute value of at least 0.1. The basic elements chosen for further testing were $\mathscr{R} = 90_{180}270_0$, $90_{225}270_{315}90_{225}$, $90_{180}360_{270}90_{180}$, $90_{180}360_{300}90_{180}$, $90_{180}180_{270}90_0180_{270}$, $90_0180_{90}90_{180}180_{270}$, $90_{90}90_{180}180_{270}90_0$ 90_{270}, $90_{270}90_090_{90}90_090_{270}90_0$, $90_0360_{90}270_{180}$.

The resulting pulse sequence (symmetry and basic element) should be robust with respect to chemical shift anisotropies, isotropic chemical shifts, and rf amplitude errors. In addition, the applied rf fields should be minimized. This is particularly important in systems where the abundant I-spins must be decoupled during the recoupling sequence.

We performed numerically exact two-spin simulations of the type shown in Fig. 2 for glycine, using the symmetries $R4_4^1$ and $R6_6^2$ together with the supercycle Eq. [12] and the basic elements listed above. The rf field amplitude was in all cases set to 38.500 kHz, leading to different spinning frequencies, depending on the choice of the basic element. We performed simulations varying the isotropic chemical shifts and chemical shift anisotropies. A sequence was chosen for experimental evaluation if there was only a small difference between simulations including and excluding chemical shifts.

We tried to choose a symmetry together with a basic element, so that not only a high transfer of longitudinal magnetization at long mixing times (quasi-equilibrium) is achieved, but also the discrepancies of oscillation frequencies for curves simulated including and ignoring chemical shifts is minimized. This is especially important, if the zero-quantum recoupling sequence should not only be used for magnetization transfer, but also for quantitative measurements of internuclear distances without the exact knowledge of the chemical shifts.

The most promising basic elements identified so far are $\mathscr{R} = 90_{180}270_0$, $90_{270}90_090_{90}90_090_{270}90_0$, $90_0360_{90}270_{180}$. The supercycled $R4_4^1$ and $R6_6^2$ sequences were tested experimentally. The best overall performance was achieved using the $R6_6^2$ symmetry together with the basic element $\mathscr{R} = 90_{180}270_0$. The symmetry $R4_4^1$ with the basic element $\mathscr{R} = 90_{270}90_090_{90}90_090_{270}90_0$ also performed well. The basic element $\mathscr{R} = 90_0360_{90}270_{180}$ performed worse experimentally, for unknown reasons.

In the following discussion, we concentrate on the following supercycled sequences:

$$SR6_6^2 = [90_{240}\ 270_{60}\ 90_{120}\ 270_{300}]^3\ [90_{120}\ 270_{300}\ 90_{240}\ 270_{60}]^3$$

$$[90_0\ 270_{180}\ 90_{240}\ 270_{60}]^3\ [90_{240}\ 270_{60}\ 90_0\ 270_{180}]^3$$

$$[90_{120}\ 270_{300}\ 90_0\ 270_{180}]^3\ [90_0\ 270_{180}\ 90_{120}\ 270_{300}]^3 \qquad [13]$$

$$SR4_4^1 = [90_{315} \; 90_{45} \; 90_{135} \; 90_{45} \; 90_{315} \; 90_{45} \; 90_{45} \; 90_{315} \; 90_{225} \; 90_{315} \; 90_{45} \; 90_{315}]^2$$

$$[90_{45} \; 90_{315} \; 90_{225} \; 90_{315} \; 90_{45} \; 90_{315} \; 90_{315} \; 90_{45} \; 90_{135} \; 90_{45} \; 90_{315} \; 90_{45}]^2$$

$$[90_{75} \; 90_{165} \; 90_{255} \; 90_{165} \; 90_{75} \; 90_{165} \; 90_{165} \; 90_{75} \; 90_{345} \; 90_{75} \; 90_{165} \; 90_{75}]^2$$

$$[90_{165} \; 90_{75} \; 90_{345} \; 90_{75} \; 90_{165} \; 90_{75} \; 90_{75} \; 90_{165} \; 90_{255} \; 90_{165} \; 90_{75} \; 90_{165}]^2$$

$$[90_{195} \; 90_{285} \; 90_{15} \; 90_{285} \; 90_{195} \; 90_{285} \; 90_{285} \; 90_{195} \; 90_{105} \; 90_{195} \; 90_{285} \; 90_{195}]^2$$

$$[90_{285} \; 90_{195} \; 90_{105} \; 90_{195} \; 90_{285} \; 90_{195} \; 90_{195} \; 90_{285} \; 90_{15} \; 90_{285} \; 90_{195} \; 90_{285}]^2,$$

$$[14]$$

where the superscripts indicate the number of repetitions of the bracketed elements.

The entire $SR6_6^2$ sequence spans 36 rotor periods and requires a rf nutation frequency of $\omega_{nut} = \omega_r$, where $\omega_r/2\pi$ is the spinning frequency in Hz. The entire $SR4_4^1$ sequence spans 24 rotor periods and requires a rf nutation frequency of $\omega_{nut} = 1.5\omega_r$.

2.5. Experimental Exchange Curves for Longitudinal Magnetization

The pulse sequence shown in Fig. 3 may be used to quantitatively follow the exchange of longitudinal magnetization between two S-spins by the $SR4_4^1$ and $SR6_6^2$ zero-quantum recoupling sequences. The sequence starts with ramped cross-polarization to enhance the S-spin magnetization (56). Longitudinal magnetization on one spin site is prepared by the free evolution interval t_1 and the following $180°$ pulse. The procedure works as follows: (i) The reference frequency is set to the mean value of the isotropic chemical shifts of the two S-spins during the evolution interval t_1, (ii) the duration is chosen so that $|\Delta\Omega_{iso}|t_1 = \pi/2$, where $|\Delta\Omega_{iso}|$ is the absolute value of the chemical shift difference, and (iii) the phase of the following $\pi/2$-pulse on the S-spins is chosen to be $5\pi/4$, if the cross polarization field on the ^{13}C has phase 0. As a result longitudinal magnetization is prepared on the more deshielded spin site. More sophisticated preparation methods exist if the chemical shift anisotropies are considerable (57, 58).

A rotor-synchronized zero-quantum recoupling sequence, denoted SRN_n^ν, is applied to the S-spins to transfer longitudinal magnetization between neighboring sites. The mixing sequence consists of q_{mix} basic elements, where q_{mix} is an even integer.

The mixing interval is therefore given by $\tau_{mix} = q_{mix}n\tau_r/N$. The longitudinal S-spin magnetization is converted into observable magnetization by a $\pi/2$ read pulse and the complex S-spin NMR signal is detected in the subsequent period.

Experimental longitudinal magnetization transfer curves for $[^{13}C_2, ^{15}N]$-glycine (98% ^{13}C, 96–99 % ^{15}N) are shown in Fig. 4. The sample was purchased from Cambridge Isotope Laboratories and used without further purification or recrystallization. The experiments were performed at a static magnetic field of $B_0 = 9.4$ T and a spinning frequency of $\omega_r/2\pi = 23.000$ kHz on a Chemagnetics Infinity-400 spectrometer using a filled 3.2-mm zirconia rotor. Longitudinal magnetization was prepared on the CO-spins using a cross-polarization contact-time of 1 ms and a t_1 interval of 16.4 μs. During the zero-quantum recoupling sequence RN_n^ν longitudinal magnetization was transferred between the CO- and the C^α-spins. Continuous wave decoupling was used with the proton nutation frequency 150 kHz during the interval t_1 and during the recoupling sequence. TPPM decoupling (59) was used during the data acquisition with a proton nutation frequency of 100 kHz. The TPPM pulses had duration 4.85 μs and phases $\pm15°$.

Figures 4a and 4b show results obtained with the $SR6_6^2$ sequence in Eq. [14]. The S-spin nutation frequency during the $SR6_6^2$ sequence was 23 kHz. The symbols in Figs. 4a and 4b show the normalized experimental peak integrals of the CO-spectral peak and the C^α-spectral peak as a function of the mixing interval τ_{mix}. The peak integrals were in all cases normalized to the CO-peak integral at $\tau_{mix} = 0$. The peak amplitudes for $\tau_{mix} = 12.5$ ms deviate unexpectedly from the other experimental points, for unknown reasons.

Figures 4c and 4d show results obtained with the $SR4_4^1$ sequence in Eq. [13]. The S-spin nutation frequency during the $SR4_4^1$ sequence was 34.5 kHz. The symbols in Figs. 4a and 4b show the normalized experimental peak integrals of the CO-spectral peak and the C^α-spectral peak as a function of the mixing interval τ_{mix}.

The solid lines in Fig. 4 are the results of accurate two-spin simulations using the interaction parameters given in the caption to Fig. 6. The simulations do not take relaxation into account. The numerical simulations reflect the oscillations in the experimentally acquired curve rather well. The relaxation loss during the recoupling sequence is slightly higher during the $SR4_4^1$ sequence compared to the $SR6_6^2$ sequence. This may be due to the fact that the mismatch between the ^1H and ^{13}C nutation frequencies of rf fields during the recoupling sequence is smaller in the case of the $SR4_4^1$ sequence.

Note that in both cases the longitudinal magnetization is rapidly transferred between the spins and then settles into a slowly-decaying quasiequilibrium state.

In order to specify the phase cycle used, denote the phases as follows: Φ_H for the proton 90° pulse, Φ_{prep} for the cross-polarization field on ^{13}C, Φ_{flip} and Φ_{read} for the ^{13}C 180° pulses, Φ_{mix} for the overall phase of the mixing sequence, Φ_{rec} and Φ_{dig} the rf receiver phase and post-digitization phase shift.
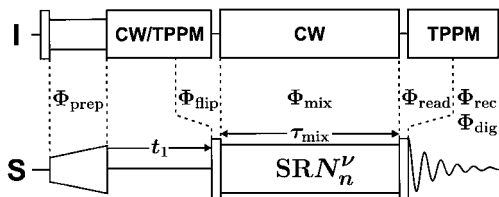

FIG. 3. Radio-frequency pulse sequence for longitudinal homonuclear magnetization transfer between spins of species S in the presence of an abundant species I with high gyromagnetic ratio. The phases Φ_{prep}, Φ_{flip}, Φ_{mix}, Φ_{read} refer to overall rf phases of the pulse sequence blocks. The rf receiver phase during signal detection is denoted Φ_{rec} and the post-digitization phase by Φ_{dig}.

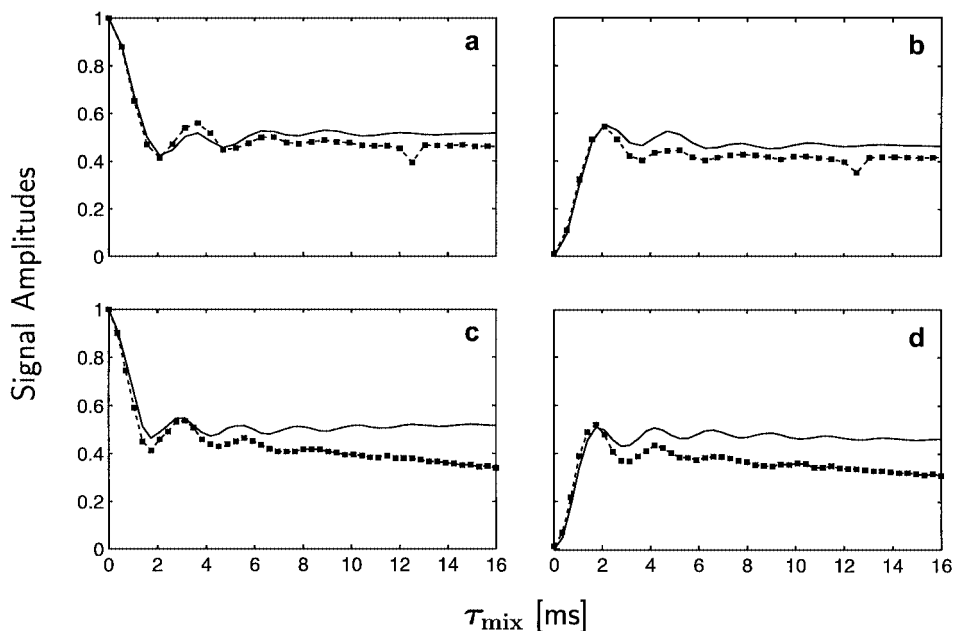**FIG. 4.** (symbols) Experimental longitudinal magnetization transfer curves for [$^{13}C_2$, ^{15}N]-glycine (98% ^{13}C, 96–99% ^{15}N) obtained at a field of $B_0 = 9.4$ T and a spinning frequency of $\omega_r/2\pi = 23.000$ kHz. (a) and (b) Normalized peak integrals of the CO peak and the C^α peak, respectively, for the SR6$_6^2$ sequence in Eq. [14]; (c) and (d) normalized peak integrals of the CO peak and the C^α peak respectively for the SR4$_4^1$ sequence in Eq. [13]. (solid lines) Two-spin numerical simulations of the transfer curves, using the parameters in the caption of Fig. 6. Powder averaging was performed using 6044 molecular orientations, chosen according to the ZCW scheme (79).

The 32-step phase cycle is specified as

$$\Phi_H = \pi \; \mathrm{floor}\left(\frac{m_t}{4}\right)$$

$$\Phi_{prep} = \pi \; \mathrm{floor}\left(\frac{m_t}{2}\right)$$

$$\Phi_{flip} = \frac{5}{4}\pi + m_t\pi$$

$$\Phi_{mix} = 0 \qquad\qquad [15]$$

$$\Phi_{read} = \frac{\pi}{2} + \frac{\pi}{2}m_t$$

$$\Phi_{rec} = 0$$

$$\Phi_{dig} = \Phi_H + \Phi_{prep} + \Phi_{read} - \Phi_{flip} + \frac{3}{4}\pi,$$

where the transient counter m_t takes the values $m_t = 0$, 1, 2, ..., 31.

3. SIMULATIONS OF ^{13}C MAGNETIZATION TRANSFER IN PROTEINS

One of the major applications of zero-quantum recoupling sequences is assignment of ^{13}C spectra by the homonuclear correlation spectroscopy of uniformly ^{13}C-labeled peptides and proteins (31–40). In order to assess the performance of the new pulse sequences in this context and to compare them with previously described sequences, we have simulated the longitudinal magnetization transfer for three typical cases, corresponding to representative spin-1/2 pairs in a labeled peptide or protein.

Figure 5 shows a diagram of ^{13}C isotropic chemical shift distributions for the CO, C^α, and C^β sites of the 20 common amino acids in peptides and proteins, assembled from the BioMagRes-Bank (BMRB) database (60). The deshielding convention is used. The typical chemical shift distributions are represented by rectangles, given by the mean chemical shift plus/minus one standard deviation. ^{13}C chemical shifts outside eight standard deviations from the mean were excluded from the statistics (60).

Simulations were performed for three representative spin pairs, with the ^{13}C isotropic chemical shifts indicated in Fig. 5. The spread of isotropic and anisotropic chemical shifts for these 3 cases is assumed to be roughly representative of the range of spin interaction parameters encountered for amino acid residues in a protein.

Case 1 corresponds to the CO and C^α sites in $^{13}C_2$-labeled glycine, with an isotropic chemical shift difference of 133.2 ppm. Case 2 corresponds to the C^α and C^β sites in [$^{13}C_2$, $^{13}C_3$]-labeled alanine. The chemical shift difference of 30.9 ppm is relatively large for a (α, β) spin pair. Case 3 corresponds to the C^α and C^β sites in [$^{13}C_2$, $^{13}C_3$]-labeled serine. In this case, the chemical shift difference of 3.4 ppm is relatively small. In all simulations, the spectrometer reference frequency was set to the mean value of the ^{13}C chemical shifts of the CO and C^α sites in glycine,
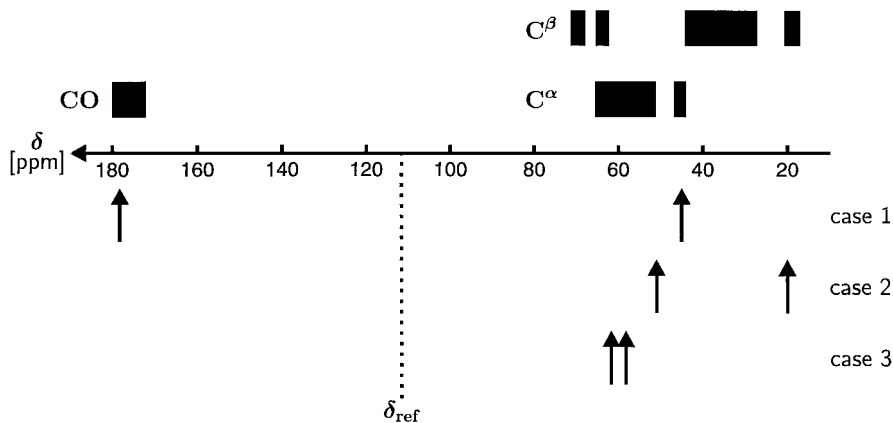
FIG. 5. (above the axis) Schematic isotropic chemical shift distributions for the CO, C^α and C^β sites of the 20 common amino acids in peptides and proteins. For each site the isotropic chemical shift distribution for the different amino acids is represented by black rectangles, spanning the range bounded by the average isotropic chemical shift plus/minus one standard deviation. The statistical data was obtained from the BioMagResBank (BMRB) database (60). Isotropic chemical shifts outside eight standard deviations from the mean were excluded from the statistics. (below the axis) ^{13}C isotropic chemical shifts for three representative spin pairs. Case 1: CO and C^α sites in glycine. For the values of the simulation parameters see the caption of Fig. 6. Case 2: C^α and C^β sites in alanine. For the simulation parameters see the caption of Fig. 7. Case 3: C^α and C^β sites in serine. For the simulation parameters see the caption of Fig. 8.

given by $\delta_{ref} = 111.6$ ppm. As may be seen in Fig. 5, the mean isotropic shifts for cases 2 and 3 are significantly off-resonance. This is a realistic scenario if ^{13}C correlation spectroscopy is attempted on a complete ^{13}C spectrum.

In all three cases, we simulated the transfer of longitudinal magnetization between the two spin sites as a function of the mixing interval τ_{mix} and magnetic field B_0. Although these simulations only involve 2-spin-1/2 systems, they are expected to give a reasonable estimate of the sequence performance in realistic circumstances. The numerical simulations of the RIL sequence were carried out using SIMPSON (86).

3.1. Case 1: Glycine Parameters

Simulations for the CO and C^α sites in glycine are shown in Fig. 6. The spin interaction parameters are given in the figure caption. The amplitude of magnetization transferred from the CO to the C^α site is plotted as a function of the mixing time τ_{mix} and the static magnetic field B_0 in the range $0 \leq B_0 \leq 23.5$ T. This corresponds to a range of ^1H Larmor frequencies of $[0, -1000$ MHz]. The value for B_0 is used to scale the isotropic chemical shifts and the chemical shift anisotropies. Typical standard values for the magnetic field, used routinely in MAS NMR, are 9.4 and 14.1 T, corresponding to ^1H Larmor frequencies of -400 and -600 MHz, respectively. The reference frequency is set to $\delta_{ref} = 111.6$ ppm, i.e., to the mean of the CO and C^α isotropic chemical shifts.

The simulations in Figs. 6a, 6b, and 6c display the performance of the $SR6_6^2$ sequence in Eq. [14], at spinning frequencies of 15.000, 23.000, and 38.500 kHz, respectively. In all cases the nutation frequency is equal to the spinning frequency. The data points were sampled at multiples of 12 basic elements, i.e., after complete $R6_6^2 R6_6^{-2}$ blocks. Figure 6a shows that for a spinning

frequency of 15.000 kHz the $SR6_6^2$ sequence performs well up to magnetic fields of about 9 T. For higher magnetic fields the performance of the sequence degrades rapidly. The operational range with respect to the magnetic field is increased with increasing spinning frequency, since the applied rf field also increases. In the case of Fig. 6b, spinning frequency 23.000 kHz, the $SR6_6^2$ sequence performs well up to magnetic fields of about 12 T. The simulations at a spinning frequency of 38.500 kHz, shown in Fig. 6c, indicate good performance at all currently accessible magnetic fields.

The simulations in Figs. 6d, 6e, and 6f display the performance of the fpRFDR sequence with simple 180_0 pulses and the XY-16 cycle at spinning frequencies of 15.000, 23.000, and 38.500 kHz, respectively. The nutation frequency of the $180°$ pulses is in all cases given by 150 kHz. The ratio of the pulse duration and the rotational period is given by (a) $\tau_p/\tau_r = 0.05$, (b) $\tau_p/\tau_r = 0.077$, and (c) $\tau_p/\tau_r = 0.128$. The rf requirement during the $180°$ pulses is relatively high, whereas the average rf requirement is moderate. In the case of glycine the magnitude of the exchanged magnetization using the fpRFDR sequence is very high except at extremely low magnetic fields (see Fig. 6d). However, the oscillation frequency of the transferred magnetization depends strongly on the external magnetic field. The dependence is strongest for low ratios τ_p/τ_r, because the scaling factor approaches zero in this case and the functioning of the sequence relies on second-order chemical shift effects. At higher ratios τ_p/τ_r the scaling factor is finite and the functioning of the sequence depends less on the chemical shifts, but the oscillation frequency of the transferred magnetization still depends on the external magnetic field. The magnetization transfer in fpRFDR is achieved by a combination of recoupled homonuclear direct dipolar couplings and homonuclear J-couplings. The J-coupling transfer is particularly important at low magnetic fields.
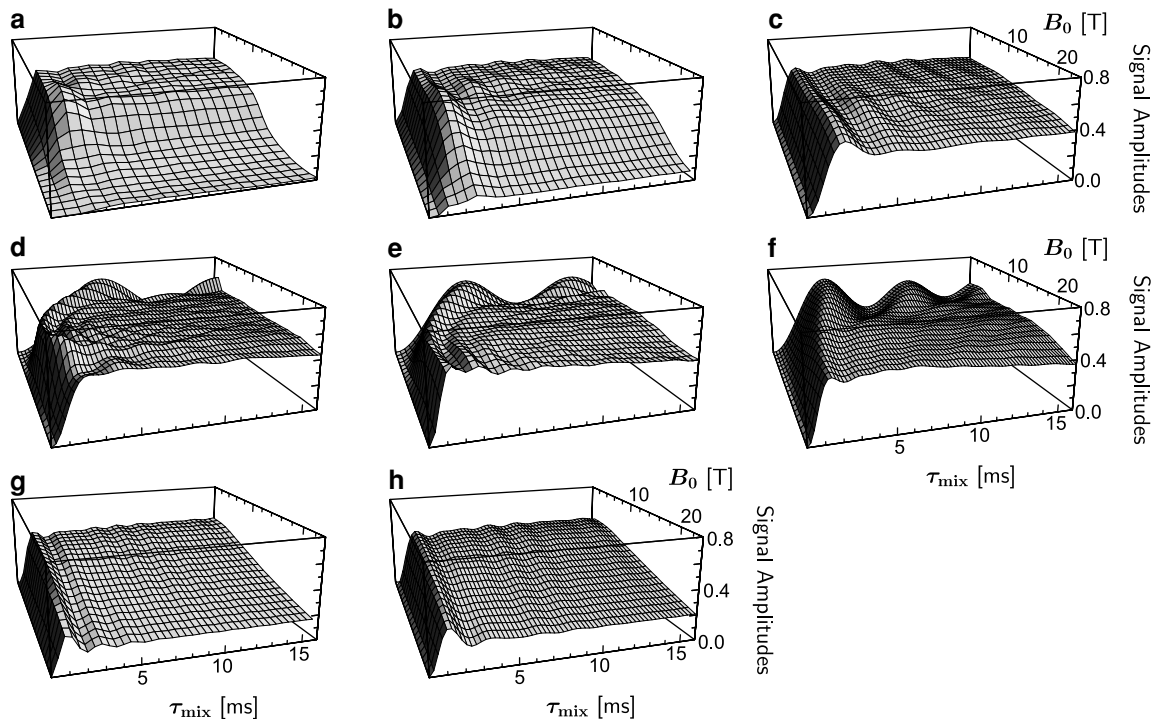
FIG. 6. Simulated transferred longitudinal magnetization from the CO site to the C^α site in glycine (case 1). *Left column* (a, d, g): Simulations at a spinning frequency of 15.000 kHz. *Middle column* (b, e, h): Simulations at a spinning frequency of 23.000 kHz. *Right column* (c, f): Simulations at a spinning frequency of 38.500 kHz. *Top row* (a, b, c): SR6$_6^2$ simulations. *Middle row* (d, e, f): fpRFDR with simple 180_0 pulses and the XY-16 phase cycle and a nutation frequency of 150.000 kHz for the $180°$ pulses. *Bottom row* (g, h): RIL simulations with $\delta = 0.75$ and nutation frequency of the strong pulses equal to 192.500 kHz. For (g) $S = 10$; for (h) $S = 6$. All simulations used powder averaging with 6044 molecular orientations, chosen according to the ZCW scheme (*79*). The parameters of glycine are taken from Ref. *80* and are as follows: The molecule-fixed frame M has its z axis along the $^{13}C^\alpha$–^{13}CO internuclear vector. The $^{13}C^\alpha$–^{13}CO dipolar coupling constant is $b/2\pi = -2135$ Hz, Euler angles $\Omega_{PM} = \{0°, 0°, 0°\}$. The J-coupling is $J = 53.1$ Hz. The reference frequency was set to $\delta_{ref} = 111.6$ ppm. $^{13}C^\alpha$-site: isotropic shift $\delta_{iso} = -66.6$ ppm, shift anisotropy $\delta_{aniso} = -19.43$ ppm (deshielding units), asymmetry parameter $\eta = 0.98$, Euler angles $\Omega_{PM} = \{99.4°, 146.0°, 138.9°\}$. ^{13}CO-site: isotropic shift $\delta_{iso} = 66.6$ ppm, shift anisotropy $\delta_{aniso} = -74.5$ ppm (deshielding units), asymmetry parameter $\eta = 0.88$, Euler angles $\Omega_{PM} = \{-0.7°, 88.5°, 52.5°\}$.

The simulations in Figs. 6g and 6h display the performance of the RIL sequence (*12, 40*). In this case, the basic building block lasts one whole rotational period, which is divided into half a rotor period of continuous rf irradiation and half a rotor period, containing strong rf pulses for refocusing the isotropic chemical shifts and chemical shift anisotropies. The ratio of the nutation frequency of the continuous rf field and the spinning frequency, denoted S, is recommended (*40*) to be larger than 10. The interval of continuous irradiation is divided into two parts. The nutation frequency of the rf field is reduced by a factor of δ in the second part. All simulations used $\delta = 0.75$ and a nutation frequency of 192.5 kHz for the strong pulses. The RIL pulse sequence generates a zero-quantum average Hamiltonian, but only if the average Hamiltonian is viewed in a tilted coordinate system, related to the standard rotating frame by a $\pi/2$ rotation around the y axis (*40*). To study the exchange of longitudinal magnetization, we therefore bracketed the whole RIL sequence by infinitely strong (ideal) $\pi/2$-pulses. The simulations in Fig. 6g were performed for a spinning frequency of 15.000 kHz and a ratio of $S = 10$, leading to a nutation frequency of 150 kHz. Figure 6h shows simulations at a spinning frequency

of 23.000 kHz. In this case, we use a ratio of $S = 6$, leading to a nutation frequency of 138.000 kHz. (A value of 10 would lead to an impractical nutation frequency of 230.000 kHz). No RIL simulations were performed at a spinning frequency of 38.500 kHz, because the rf field is too high for practical applications, even in the case of $S = 6$.

The RIL sequence performs best at a spinning frequency of 23.000 kHz, even though in this case the chosen value $S = 6$ is smaller than the minimum recommended value of $S = 10$. In both cases, Figs. 6g and 6h, the performance of the RIL sequence degrades steadily with increasing external magnetic field. The scaling factor of RIL is relatively high, leading to fast oscillations, which are roughly field-independent.

3.2. Case 2: Alanine Parameters

Simulation results for the C^α and C^β sites in alanine are shown in Fig. 7. The reference frequency is set to the same value as for the glycine simulations, as discussed above.

Figures 7a, 7b, and 7c display the performance of the SR6$_6^2$ sequence at spinning frequencies of 15.000, 23.000, and
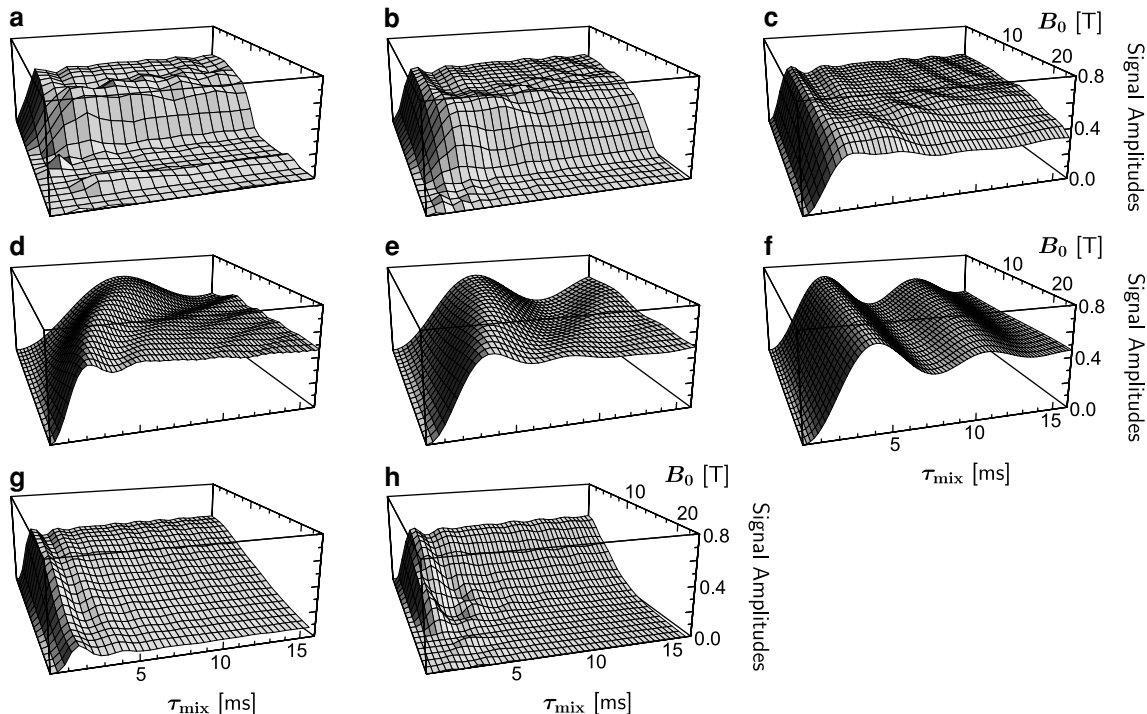
FIG. 7. Simulated transferred longitudinal magnetization from the C^α to the C^β sites in alanine. The assignment of the plots and the pulse sequence parameters are as in Fig. 6. The parameters of alanine are taken from Ref. *81* and are as follows: The molecule-fixed frame M coincides with the crystallographic reference frame of Ref. *82*. The $^{13}C^\alpha$–$^{13}C^\beta$ dipolar coupling constant is $b/2\pi = -2156$ Hz, Euler angles $\Omega_{PM} = \{0°, 78.4°, 144.7°\}$. The J-coupling is $J = 35$ Hz (*83*). The reference frequency was set to $\delta_{ref} = 111.6$ ppm. $^{13}C^\alpha$-site: isotropic shift $\delta_{iso} = -60.7$ ppm, shift anisotropy $\delta_{aniso} = -19.67$ ppm (deshielding units), asymmetry parameter $\eta = 0.437$, Euler angles $\Omega_{PM} = \{81.7°, 24.5°, 29.1°\}$. $^{13}C^\beta$-site: isotropic shift $\delta_{iso} = -91.6$ ppm, shift anisotropy $\delta_{aniso} = -11.7$ ppm (deshielding units), asymmetry parameter $\eta = 0.76$, Euler angles $\Omega_{PM} = \{-52.9°, 77.4°, 140.5°\}$.

38.500 kHz, respectively. Figure 7a shows that at a spinning frequency of 15.000 kHz the $SR6_6^2$ sequence performs well up to magnetic fields of about 8 T, whereas the performance degrades rapidly at higher magnetic fields. At a spinning frequency of 23.000 kHz, Fig. 7b, the $SR6_6^2$ sequence performs well up to magnetic fields of about 10 T. Figure 7c shows that at a spinning frequency of 38.500 kHz, the $SR6_6^2$ sequence performs reasonable well over the whole range of magnetic fields, even though in general the performance for case 2 is slightly worse than for case 1.

The simulations in Figs. 7d, 7e, and 7f display the performance of the fpRFDR sequence at spinning frequencies of 15.000, 23.000, and 38.500 kHz, respectively. The most important difference to case 1 (glycine) is the reduced oscillation frequency of the transferred longitudinal magnetization. This illustrates the fact that fpRFDR is strongly dependent on the chemical shift differences between coupled spins. Additional simulations (not shown) indicate that the magnetization transfer has a strong J-coupling component.

The simulations in Figs. 7g and 7h display the performance of the RIL sequence at spinning frequencies of 15.000 and 23.000 kHz, respectively. The pulse sequence parameters are the same as for case 1 (glycine). The most prominent observation here is that RIL fails at moderate to high magnetic fields, in

the case of the alanine (C^α, C^β) spin pair, in which both isotropic shifts have the same sign of resonance offset.

3.3. Case 3: Serine Parameters

Figure 8 shows the corresponding simulations for the case of the C^α and C^β sites in serine. The reference frequency is set to the same value as for the glycine simulations, as discussed above.

Figures 8a, 8b, and 8c display the performance of the $SR6_6^2$ sequence at spinning frequencies of 15.000, 23.000, and 38.500 kHz, respectively. Figure 8a shows that at a spinning frequency of 15.000 kHz the $SR6_6^2$ sequence performs well up to magnetic fields of about 12 T, whereas the performance degrades rapidly at higher magnetic fields. At a spinning frequency of 23.000 kHz, Fig. 8b, the $SR6_6^2$ sequence performs well up to magnetic fields of about 16 T. Figure 7(c) shows that at a spinning frequency of 38.500 kHz, the $SR6_6^2$ sequence again performs well over all currently available magnetic fields.

The simulations in Figs. 8d, 8e, and 8f display the performance of the fpRFDR sequence at spinning frequencies of 15.000, 23.000, and 38.500 kHz, respectively. Since the ^{13}C chemical shift difference of the C^α and C^β sites is very small in this case, the oscillation frequency of the transferred longitudinal magnetization is also very small and depends strongly on the J-coupling,
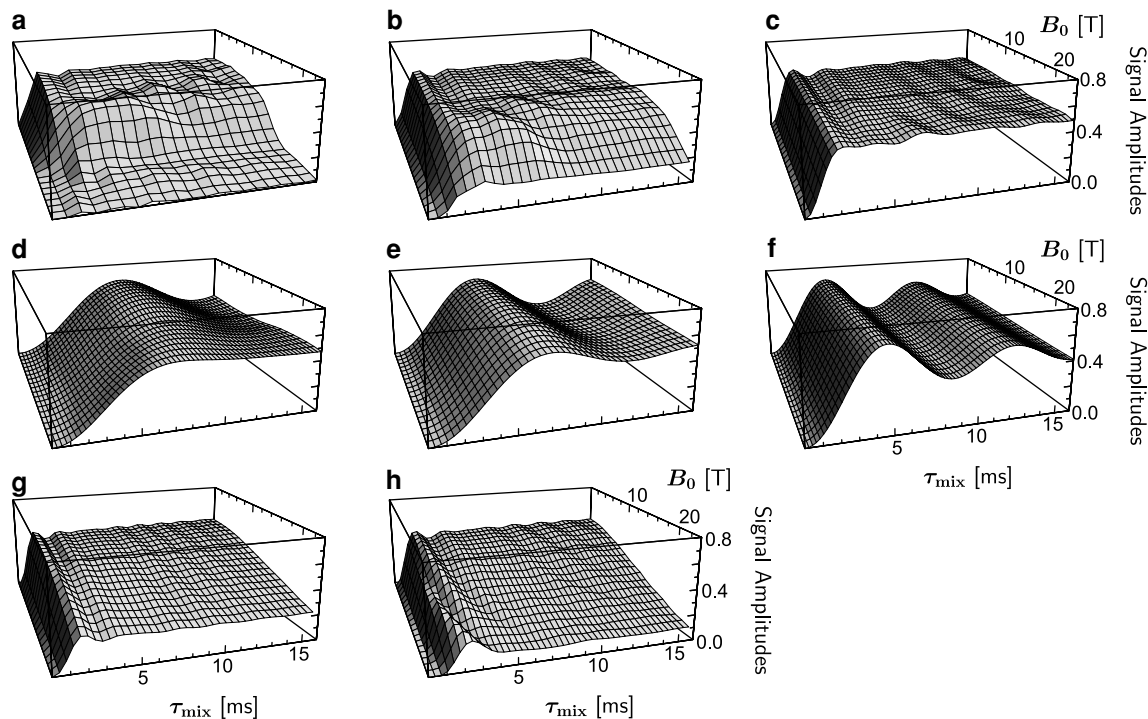
FIG. 8. Simulated transferred longitudinal magnetization from the C^α to the C^β sites in serine. The assignment of the plots and the pulse sequence parameters are as in Fig. 6. The parameters of serine are taken from Ref. *84* and are as follows: The molecule-fixed frame M coincides with the crystallographic reference frame of Ref. *85*. The $^{13}C^\alpha$–$^{13}C^\beta$ dipolar coupling constant is $b/2\pi = -2169$ Hz, Euler angles $\Omega_{PM} = \{0°, 84.2°, 70.0°\}$. The J-coupling is $J = 36.4$ Hz (*83*). The reference frequency was set to $\delta_{\mathrm{ref}} = 111.6$ ppm. $^{13}C^\alpha$-site: isotropic shift $\delta_{\mathrm{iso}} = -53.3$ ppm, shift anisotropy $\delta_{\mathrm{aniso}} = -14.1$ ppm (deshielding units), asymmetry parameter $\eta = 0.67$, Euler angles $\Omega_{PM} = \{176.5°, 79.1°, 168.8°\}$. $^{13}C^\beta$-site: isotropic shift $\delta_{\mathrm{iso}} = -49.9$ ppm, shift anisotropy $\delta_{\mathrm{aniso}} = -27.67$ ppm (deshielding units), asymmetry parameter $\eta = 0.72$, Euler angles $\Omega_{PM} = \{108.8°, 20.7°, 62.9°\}$.

the magnetic field and the ratio τ_p/τ_r of pulse duration and rotor period.

The simulations in Figs. 8g and 8h display the performance of the RIL sequence at spinning frequencies of 15.000 and 23.000 kHz, respectively. The performance degrades at high magnetic fields, but not as strongly as for case 2.

3.4. Discussion

The simulations reveal the strong and weak sides of the three pulse sequences in the context of ^{13}C recoupling.

The low rf requirement of the $SR6_6^2$ sequence in Eq. [14] makes it suitable for application at very high spinning frequencies. The simulations at a spinning frequency of 38.500 kHz show good performance for all types of $^{13}C_2$ spin pairs at all currently accessible magnetic fields. The results for a spinning frequency of 23.000 kHz show that the performance of the $SR6_6^2$ sequence is good for all magnetic fields up to about 12 T. This corresponds to a proton Larmor frequency of about -510 MHz. At a spinning frequency of 15.000 kHz, the performance is good for all magnetic fields up to about 9 T, which corresponds to a proton Larmor frequency of about -380 MHz.

The strong side of the fpRFDR sequence with simple 180_0 pulses is the generally high amplitude of transferred magne-

tization. The drawback is the strong dependence of the oscillation frequency on the isotropic chemical shifts, chemical shift anisotropies, J-couplings, and pulse sequence parameters. This makes it difficult to control the scope of the magnetization exchange, if the spin system consists of spins with a spread of chemical shifts. In addition, the strong participation of the J-couplings needs to be taken into account when interpreting fpRFDR exchange results. A quantitative analysis of the transfer curves would require detailed knowledge of the J-couplings, and the isotropic and anisotropic chemical shifts.

The RIL sequence performs best at lower spinning frequencies, so that the requirement $S = 10$ can be fulfilled. At high spinning frequencies (23.000 kHz), the sequence sometimes fails when the magnetic field is also high (see Fig. 7h). The RIL sequence cannot realistically be implemented at very high spinning frequencies.

In conclusion we recommend the use of the $SR6_6^2$ sequence at very high spinning frequencies, where it functions well over all realistic scenarios encountered in the correlation spectroscopy of [U-^{13}C]-labeled proteins. In this case the transfer curves are much less dependent on the chemical shifts than the fpRFDR transfer curves. The $SR6_6^2$ sequence is also recommended for low to moderate magnetic fields when using a spinning frequency of around 20.000 kHz. At lower spinning frequencies of

15.000 kHz or less, RIL is probably a better alternative at least at moderate magnetic fields. fpRFDR with simple 180_0 pulses is a good alternative over a wide range of conditions, but the results are strongly dependent on chemical shifts and J-couplings and must be interpreted with caution.

It should also be possible to choose the basic element $\mathcal{R}$ so as to provide broadband zero-quantum recoupling with an acceptable scaling factor at moderate to low spinning frequencies. However, so far, we did not succeed in discovering acceptable sequences.

4. EXPERIMENTAL DEMONSTRATIONS

The pulse sequence shown in Fig. 3 may be used to acquire two-dimensional homonuclear correlation spectra. Such spectra correlate the isotropic chemical shifts of dipolar-coupled homonuclei and are used for the assignment of MAS NMR spectra (61).

Figures 9 and 10 show experimental two-dimensional correlation spectra obtained on a sample of [98%-U-^{13}C]-L-tyrosine at a field $B_0 = 9.4$ T. The sample was purchased from Cambridge Isotope Laboratories and used without further purification. The experiments were performed on a Chemagnetics Infinity-400 spectrometer using a filled 3.2 mm zirconia rotor.

The pulse sequence in Fig. 3 was used, with 256 increments of the interval t_1 in steps of 15 μs. The data matrix $s(t_1, t_2)$ was subjected to a complex Fourier transform in the t_2 dimension, and a cosine Fourier transform in the t_1 dimension, in order to obtain the 2D spectrum $S(\omega_1, \omega_2)$.

The spectra in Figs. 9 and 10 were obtained using a cross polarization interval of 800 μs. The zero-quantum recoupling was achieved using the SR6$_6^2$ sequence in Eq. [14]. Continuous-wave proton decoupling was used during the recoupling sequence with a proton nutation frequency of 150 kHz. TPPM decoupling (59) with a proton nutation frequency of 104 kHz was used during the evolution interval t_1 and the data acquisition. The TPPM pulse
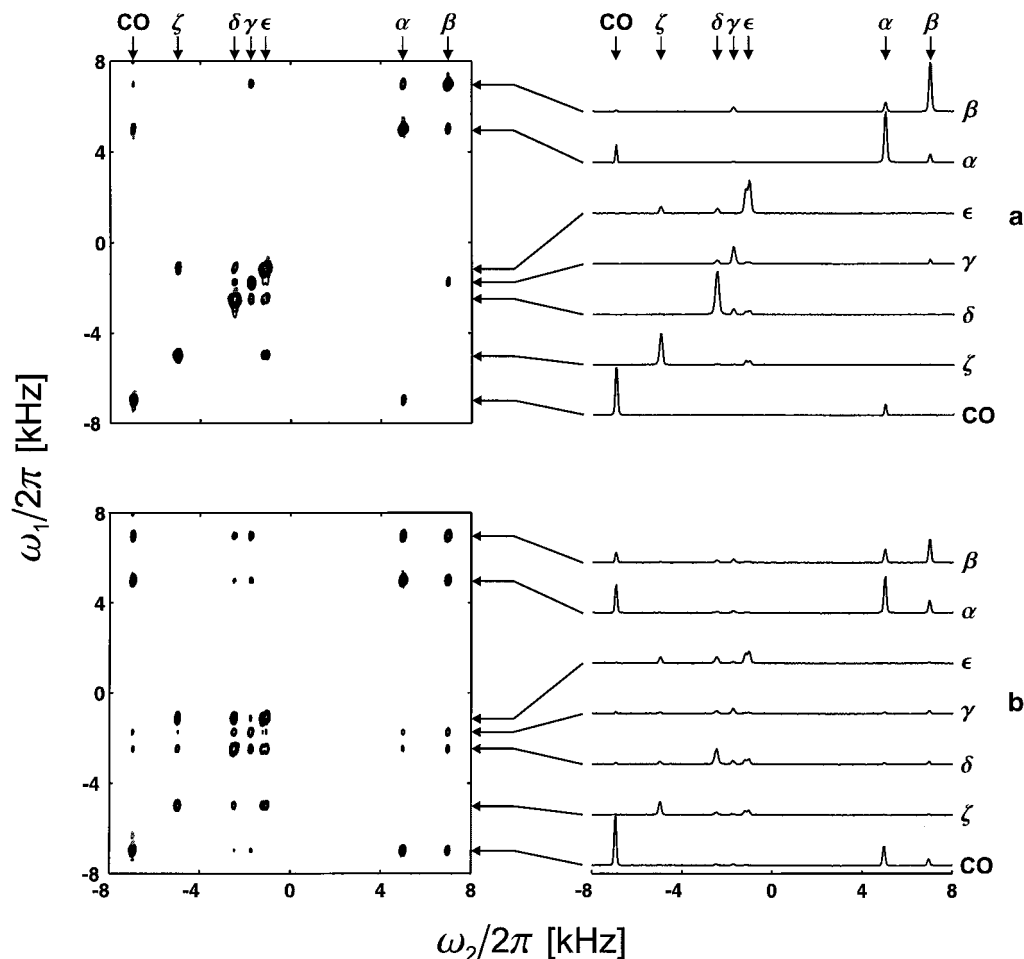

FIG. 9. Experimental 2D homonuclear correlation ^{13}C spectra of [98%-U-^{13}C]-L-tyrosine, at a field of $B_0 = 9.4$ T and a spinning frequency of $\omega_r/2\pi = $ 15.000 kHz, obtained using the pulse sequence in Fig. 3 with SR6$_6^2$ as the homonuclear zero-quantum recoupling sequence. The mixing intervals are given by (a) $\tau_{\text{mix}} = 0.8$ ms and (b) $\tau_{\text{mix}} = 9.6$ ms.
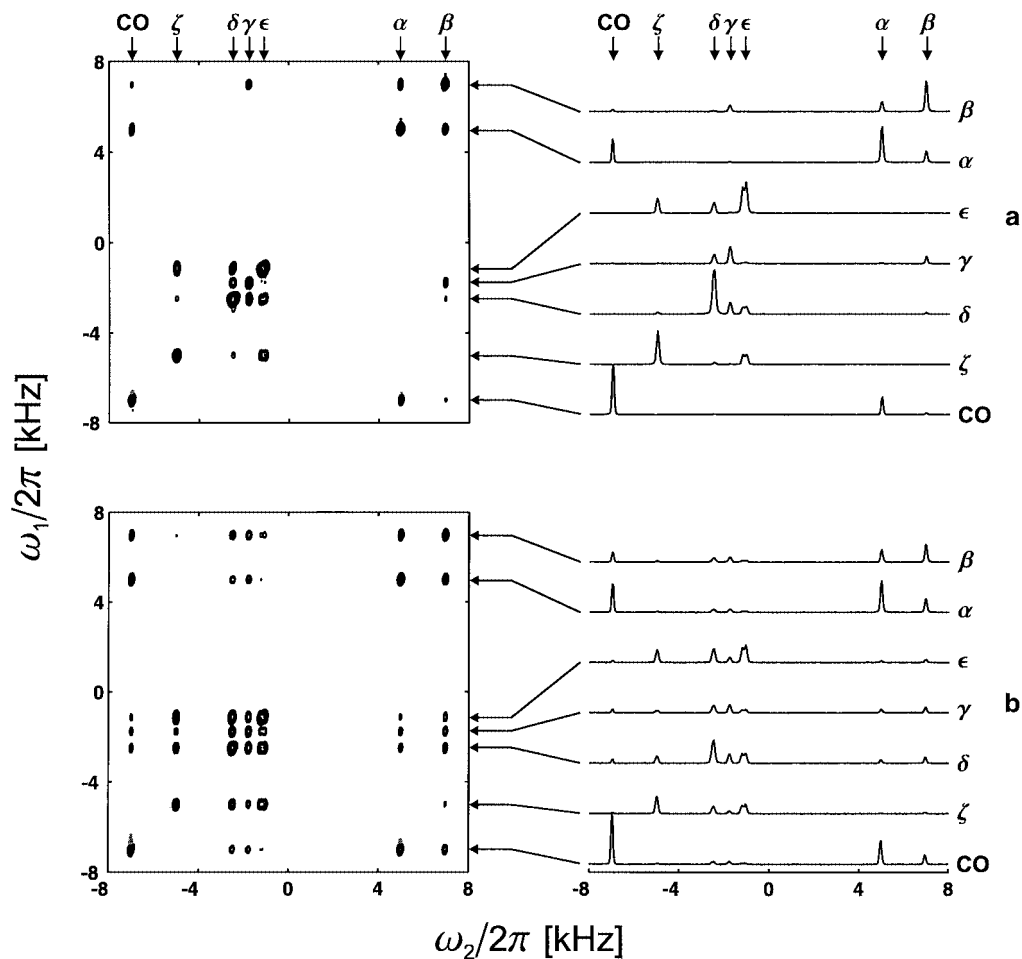
FIG. 10. Experimental 2D homonuclear correlation ^{13}C spectra of [98%-U-^{13}C]-L-tyrosine, at a field of $B_0 = 9.4$ T and a spinning frequency of $\omega_r/2\pi = 23.000$ kHz, obtained using the pulse sequence in Fig. 3 with SR6$_6^2$ as the homonuclear zero-quantum recoupling sequence. The mixing intervals are given by (a) $\tau_{mix} = 1.0$ ms and (b) $\tau_{mix} = 9.9$ ms.

durations and rf phases were ($5.0\ \mu$s, $\pm 17°$) in Fig. 9 and ($4.8\ \mu$s, $\pm 23°$) in Fig. 10.

The two-dimensional spectra shown in Fig. 9 were obtained at a spinning frequency of $\omega_r/2\pi = 15.000$ kHz. The S-spin nutation frequency during the SR6$_6^2$ sequence was 15 kHz. For the spectrum in Fig. 9a the recoupling sequence consisted of a total of $q_{mix} = 12$ basic elements, leading to a total mixing interval of $\tau_{mix} = 0.8$ ms. Figure 9b shows the spectrum for $q_{mix} = 144$, corresponding to a mixing interval of $\tau_{mix} = 9.6$ ms.

The results shown in Fig. 10 were acquired at a spinning frequency of $\omega_r/2\pi = 23.000$ kHz. The evolution interval t_1 was incremented in steps of $14.4\ \mu$s. The S-spin nutation frequency during the R6$_6^2$ sequence was 23 kHz. For the result in Fig. 10a the recoupling sequence consisted of a total of $q_{mix} = 24$ basic elements, leading to a total mixing interval of $\tau_{mix} = 1.0$ ms. Figure 9b shows the result for $q_{mix} = 228$, corresponding to a mixing interval of $\tau_{mix} = 9.9$ ms.

The short mixing interval spectra in Figs. 9a and 10a show mainly diagonal peaks and cross-peaks between neighboring

^{13}C-sites in tyrosine. All possible one-bond correlations are visible. The long mixing interval spectra in Figs. 9b and 10b on the other hand, show cross-peaks between all the ^{13}C-sites in tyrosine.

Although the distribution of peak amplitudes is somewhat more even at 23.000 kHz spinning frequency, compared to 15.000 kHz spinning frequency, the 15.000 kHz spectrum at short mixing time (Fig. 9a) is still of reasonable quality. Altogether, this underlines our expectation that the main areas of application of the zero-quantum recoupling sequences discussed here will include fast sample spinning and high magnetic fields.

The short mixing time spectra (Figs. 9a and 10a) should be compared with previously published double-quantum spectra obtained using the SC14 sequence at a spinning frequency of 20.000 kHz (47). In our experience double-quantum spectra are cleaner, and the amplitude of the informative peaks is similar in the two experiments. In addition, double-quantum spectra do not suffer from the participation of the J-couplings in the magnetization transfer process (47). Double-quantum spectroscopy

is therefore recommended for establishing short-range correlations. Single-quantum correlation spectra using zero-quantum mixing Hamiltonians may be most useful in the long mixing time case, as in Figs. 9b and 10b. In multiple-spin systems, the extended quasi-equilibrium state leads to strong long-range and relayed correlations, which may be useful for qualitative assignments in some cases. However, this regime is often difficult to interpret quantitatively.

The results in Figs. 9 and 10 were obtained using a 8-step phase cycle with implementation of time-proportional phase incrementation (TPPI) to obtain pure absorption two-dimensional spectra with discrimination of positive and negative ω_1 frequencies (61). The phase cycle is specified using the transient counter m_t, and the evolution increment counter, denoted m_{ev}, which is incremented between different values of t_1. The transient counter takes the values $m_t = 0, 1, \ldots, 7$ and the phase specifications are

$$
\begin{aligned}
\Phi_H &= 0 \\
\Phi_{prep} &= \pi \, \text{floor}\left(\frac{m_t}{4}\right) + \frac{\pi}{2}m_{ev} \\
\Phi_{flip} &= \frac{3}{2}\pi \\
\Phi_{mix} &= 0 \qquad\qquad\qquad\qquad [16] \\
\Phi_{read} &= \frac{\pi}{2} + \frac{\pi}{2}m_t \\
\Phi_{rec} &= 0 \\
\Phi_{dig} &= \Phi_{prep} + \Phi_{read} - \frac{\pi}{2}.
\end{aligned}
$$

5. CONCLUSIONS

In this paper we have shown how symmetry arguments may be used to help construct zero-quantum homonuclear recoupling sequences in magic-angle-spinning solid-state NMR. A table of suitable symmetries is given which lead to zero-quantum recoupling in the first order average Hamiltonian. The performance of these sequences is stabilized by implementing supercycles. A number of specific pulse sequences is given. One of the most promising candidates, called $SR6_6^2$, is demonstrated experimentally by obtaining longitudinal magnetization transfer curves for $[^{13}C_2, {}^{15}N]$-glycine at a spinning frequency of 23.000 kHz and by the two-dimensional ^{13}C correlation spectroscopy of $[U-^{13}C]$-L-tyrosine at spinning frequencies of 15.000 and 23.000 kHz.

The performance of several different zero-quantum recoupling sequences has been simulated for three test cases representing conditions typical for ^{13}C correlation spectroscopy in $[U-^{13}C]$-labeled proteins. The $SR6_6^2$ sequence gives very good performance over all currently accessible magnetic field strengths, providing the spinning frequency is very high (sim-

ulated at 38.500 kHz). At the more readily accessible spinning frequency of 23.000 kHz, its performance is adequate for work at magnetic fields up to around 12 T. Work is in progress for the development of pulse sequences with good broadband performance at more moderate spinning frequencies.

Possible applications of the zero-quantum recoupling sequence $SR6_6^2$ include the quantitative estimation of internuclear distances (8, 62–66) and excitation of multiple-quantum coherences (9, 58, 63, 67–70). Recently, the excitation of high-order ^{13}C multiple-quantum coherence in magic-angle-spinning solids was demonstrated using the fpRFDR sequence (70). The higher scaling factor of $SR6_6^2$ should facilitate these experiments.

In summary, we have demonstrated another promising domain of application of the recoupling symmetry theory, complementing the existing applications to homonuclear double-quantum recoupling (14–19, 47), heteronuclear recoupling (18, 20, 21, 71–75), heteronuclear decoupling (18, 46), generalized Hartmann–Hahn recoupling (48), selection of isotropic chemical shifts (49), and J-couplings (18, 76–78). For a review of the current status of symmetry-aided pulse sequence design in MAS solid state NMR see Ref. 53.

REFERENCES

1. D. P. Raleigh, M. H. Levitt, and R. G. Griffin, Rotational resonance in solid state NMR, *Chem. Phys. Lett.* **146,** 71–76 (1988).

2. Z.-H. Gan and D. M. Grant, Pseudo-spin rotational resonance and homonuclear dipolar N.M.R. of rotating solids, *Mol. Phys.* **67,** 1419–1430 (1989).

3. M. H. Levitt, D. P. Raleigh, F. Creuzet, and R. G. Griffin, Theory and simulations of homonuclear spin pair systems in rotating solids, *J. Chem. Phys.* **90,** 6347–6364 (1990).

4. T. Karlsson and M. H. Levitt, Longitudinal rotational resonance echoes in solid state nuclear magnetic resonance: Investigation of zero quantum spin dynamics, *J. Chem. Phys.* **109,** 5493–5507 (1998).

5. M. Helmle, Y. K. Lee, P. J. E. Verdegem, X. Feng, T. Karlsson, J. Lutgenburg, H. J. M. de Groot, and M. H. Levitt, Anomalous rotational resonance spectra in magic-angle-spinning NMR, *J. Magn. Reson.* **140,** 379–403 (1999).

6. K. Nomura, K. Takegoshi, T. Terao, K. Uchida, and M. Kainosho, Determination of the complete structure of a uniformly labeled molecule by rotational resonance solid-state NMR in the tilted rotating frame, *J. Am. Chem. Soc.* **121,** 4064–4065 (1999).

7. T. Gullion and J. Schaefer, Detection of weak heteronuclear dipolar coupling by rotational-echo double-resonance nuclear magnetic resonance, *Adv. Magn. Reson.* **13,** 57–83 (1989).

8. R. Tycko and G. Dabbagh, Measurement of nuclear magnetic dipole-dipole couplings in magic angle spinning NMR, *Chem. Phys. Lett.* **173,** 461–465 (1990).

9. R. Tycko and G. Dabbagh, Double-quantum filtering in magic-angle-spinning NMR spectroscopy: An approach to spectral simplification and molecular structure determination, *J. Am. Chem. Soc.* **113,** 9444–9448 (1991).

10. D. M. Gregory, D. J. Mitchell, J. A. Stringer, S. Kiihne, J. C. Shiels, J. Callahan, M. A. Mehta, and G. P. Drobny, Windowless dipolar recoupling: The detection of weak dipolar couplings between spin 1/2 nuclei with large chemical shift anisotropies, *Chem. Phys. Lett.* **246,** 654–663 (1995).

11. M. Baldus, M. Tomaselli, B. Meier, and R. R. Ernst, Broadband polarization-transfer experiments for rotating solids, *Chem. Phys. Lett.* **230,** 329–336 (1994).

12. M. Baldus, R. J. Iuliucci, and B. H. Meier, Probing through-bond connectivities and through-space distances in solids by magic-angle-spinning nuclear magnetic resonance, *J. Am. Chem. Soc.* **119,** 1121–1124 (1997).

13. N. C. Nielsen, H. Bildsøe, H. J. Jakobsen, and M. H. Levitt, Double-quantum homonuclear rotary resonance: Efficient dipolar recovery in magic-angle spinning nuclear magnetic resonance, *J. Chem. Phys.* **101,** 1805–1812 (1994).

14. Y. K. Lee, N. D. Kurur, M. Helmle, O. G. Johannessen, N. C. Nielsen, and M. H. Levitt, Efficient dipolar recoupling in the NMR of rotating solids. A sevenfold symmetric radiofrequency pulse sequence, *Chem. Phys. Lett.* **242,** 304–309 (1995).

15. C. M. Rienstra, M. E. Hatcher, L. J. Mueller, B. Sun, S. W. Fesik, and R. G. Griffin, Efficient multispin homonuclear double-quantum recoupling for magic-angle spinning NMR: ^{13}C–^{13}C correlation spectroscopy of U-^{13}C-Eryhromycin A, *J. Am. Chem. Soc.* **120,** 10,602–10,612 (1998).

16. M. Hohwy, H. J. Jakobsen, M. Edén, M. H. Levitt, and N. C. Nielsen, Broadband dipolar recoupling in the nuclear magnetic resonance of rotating solids: A compensated C7 pulse sequence, *J. Chem. Phys.* **108,** 2686–2694 (1998).

17. M. Hohwy, C. M. Rienstra, C. P. Jaroniec, and R. G. Griffin, Fivefold symmetric homonuclear dipolar recoupling in rotating solids: Application to double quantum spectroscopy, *J. Chem. Phys.* **110,** 7983–7992 (1999).

18. M. Carravetta, M. Edén, X. Zhao, A. Brinkmann, and M. H. Levitt, Symmetry principles for the design of radiofrequency pulse sequences in the nuclear magnetic resonance of rotating solids, *Chem. Phys. Lett.* **321,** 205–215 (2000).

19. M. Carravetta, M. Edén, O. G. Johannessen, H. Luthman, P. J. E. Verdegem, J. Lugtenburg, A. Sebald, and M. H. Levitt, Estimation of carbon-carbon bond lengths and medium-range internuclear distances by solid-state nuclear magnetic resonance, *J. Am. Chem. Soc.* **123,** 10,628–10,638 (2001).

20. X. Zhao, M. Edén, and M. H. Levitt, Recoupling of heteronuclear dipolar interactions in solid-state NMR using symmetry-based pulse sequences, *Chem. Phys. Lett.* **342,** 353–361 (2001).

21. X. Zhao, J. E. Sudmeier, W. W. Bachovchin, and M. H. Levitt, Measurement of NH bond lengths by fast magic-angle spinning solid-state NMR spectroscopy: A new method for the quantification of hydrogen bonds, *J. Am. Chem. Soc.* **123,** 11,097–11,098 (2001).

22. Y. Ishii, T. Terao, and M. Kainosho, Relayed anisotropy correlation NMR: Determination of dihedral angles in solids, *Chem. Phys. Lett.* **256,** 133–140 (1996).

23. X. Feng, Y. K. Lee, D. Sandström, M. Edén, H. Maisel, A. Sebald, and M. H. Levitt, Direct determination of a molecular torsional angle by solid-state NMR, *Chem. Phys. Lett.* **257,** 314–320 (1996).

24. X. Feng, M. Edén, A. Brinkmann, H. Luthman, L. Eriksson, A. Gräslund, O. N. Antzutkin, and M. H. Levitt, Direct determination of a peptide torsional angle ψ by double-quantum solid-state NMR, *J. Am. Chem. Soc.* **119,** 12,006–12,007 (1997).

25. M. Hong, J. D. Gross, and R. G. Griffin, Site-resolved determination of peptide torsion angle ϕ from the relative orientations of backbone N–H and C–H bonds by solid-state NMR, *J. Phys. Chem. B* **101,** 5869–5874 (1997).

26. P. R. Costa, J. D. Gross, M. Hong, and R. G. Griffin, Solid-state NMR measurement of ψ in peptides: a NCCN 2Q-heteronuclear local field experiment, *Chem. Phys. Lett.* **280,** 95–103 (1997).

27. T. Fujiwara, T. Shimomura, and H. Akutsu, Multidimensional solid-state nuclear magnetic resonance for correlating anisotropic interactions under magic-angle spinning conditions, *J. Magn. Reson.* **124,** 147–153 (1997).

28. Y. Ishii, K. Hirao, T. Terao, T. Terauchi, M. Oba, K. Nishiyama, and M. Kainosho, Determination of peptide ϕ angles in solids by relayed anisotropy correlation NMR, *Solid State NMR* **11,** 169–175 (1998).

29. S. Ravindranathan, X. Feng, T. Karlsson, G. Widmalm, and M. H. Levitt, Investigation of carbohydrate conformation in solution and in powders by double-quantum NMR, *J. Am. Chem. Soc.* **122,** 1102–1115 (2000).

30. S. Ravindranathan, T. Karlsson, K. Lycknert, G. Widmalm, and M. H. Levitt, Conformation of the glycosidic linkage in a disaccharide investigated by double-quantum solid-state NMR, *J. Magn. Reson.* **151,** 136–141 (2001).

31. H. J. M. de Groot, Solid-state NMR spectroscopy applied to membrane proteins, *Curr. Opin. Struct. Biol.* **10,** 593–600 (2000).

32. R. Tycko, Biomolecular solid state NMR: Advances in structural methodology and applications to peptide and protein fibrils, *Annu. Rev. Phys. Chem.* **52,** 575–606 (2001).

33. G. J. Boender, J. Raap, S. Prytulla, H. Oschkinat, and H. J. M. de Groot, MAS NMR structure refinement of uniformly ^{13}C enriched chlorophyll a/water aggregates with 2D dipolar correlation spectroscopy, *Chem. Phys. Lett.* **237,** 502–508 (1995).

34. T. A. Egorova-Zachernyuk, B. van Rossum, G.-J. Boender, E. Franken, J. Ashurst, J. Raap, P. Gast, A. J. Hoff, H. Oschkinat, and H. J. M. de Groot, Characterization of pheophytin ground states in rhodobacter sphaeroides R26 photosynthetic reaction centers from multispin pheophytin enrichment and 2-D ^{13}C MAS NMR dipolar correlation spectroscopy, *Biochemistry* **36,** 7513–7519 (1997).

35. B.-J. van Rossum, G. J. Boender, F. M. Mulder, J. Raap, T. S. Balaban, A. Holzwarth, K. Schaffner, S. Prytulla, H. Oschkinat, and H. J. M. de Groot, Multidimensional CP-MAS ^{13}C NMR of uniformly enriched chlorophyll, *Spectrochim. Acta A* **54,** 1167–1176 (1998).

36. M. T. Zell, B. E. Padden, D. J. W. Grant, M.-C. Chapeau, I. Prakash, and E. J. Munson, Two-dimensional high-speed CP/MAS NMR spectroscopy of polymorphs. 1. Uniformly ^{13}C-labeled aspartame, *J. Am. Chem. Soc.* **121,** 1372–1378 (1999).

37. J. Pauli, B. van Rossum, H. Förster, H. J. M. de Groot, and H. Oschkinat, Sample optimization and identification of signal patterns of amino acid side chains in 2D RFDR spectra of the α-spectrin SH3 domain, *J. Magn. Reson.* **143,** 411–416 (2000).

38. A. McDermott, T. Polenova, A. Bockmann, K. W. Zilm, E. K. Paulsen, R. W. Martin, and G. T. Montelione, Partial NMR assignments for uniformly (^{13}C, ^{15}N)-enriched BPTI in the solid state, *J. Biomol. NMR* **16,** 209–219 (2000).

39. J. Pauli, M. Baldus, B. van Rossum, H. J. M. de Groot, and H. Oschkinat, Backbone and side-chain ^{13}C and ^{15}N signal assignments of the α-spectrin SH3 domain by magic angle spinning solid-state NMR at 17.6 tesla, *Chembiochem* **2,** 272–281 (2001).

40. M. Baldus and B. H. Meier, Broadband polarization transfer under magic-angle spinning: Application to total through-space-correlation NMR spectroscopy, *J. Magn. Reson.* **128,** 172–193 (1997).

41. T. Fujiwara, A. Ramamoorthy, K. Nagayama, K. Hioka, and T. Fujito, Dipolar HOHAHA under MAS conditions for solid-state NMR, *Chem. Phys. Lett.* **212,** 81–84 (1993).

42. A. E. Bennett, J. H. Ok, R. G. Griffin, and S. Vega, Chemical shift correlation spectroscopy in rotating solids: Radio frequency-driven dipolar recoupling and longitudinal exchange, *J. Chem. Phys.* **96,** 8624–8627 (1992).

43. T. Gullion and S. Vega, A simple magic angle spinning NMR experiment for the dephasing of rotational echoes of dipolar coupled homonuclear spin pairs, *Chem. Phys. Lett.* **194,** 423–428 (1992).

44. A. E. Bennett, C. M. Rienstra, J. M. Griffiths, W. Zhen, P. T. Lansbury, Jr., and R. G. Griffin, Homonuclear radio frequency-driven recoupling in rotating solids, *J. Chem. Phys.* **108,** 9463–9479 (1998).

45. Y. Ishii, ^{13}C–^{13}C dipolar recoupling under very fast magic angle spinning in solid-state nuclear magnetic resonance: Applications to distance measurements, spectral assignments, and high-throughput secondary structure determination, *J. Chem. Phys.* **114,** 8473–8483 (2001).

46. M. Edén and M. H. Levitt, Pulse sequence symmetries in the nuclear magnetic resonance of spinning solids: Application to heteronuclear decoupling, *J. Chem. Phys.* **111,** 1511–1519 (1999).

47. A. Brinkmann, M. Edén, and M. H. Levitt, Synchronous helical pulse sequences in magic-angle spinning nuclear magnetic resonance: Double quantum recoupling of multiple-spin systems, *J. Chem. Phys.* **112,** 8539–8554 (2000).

48. A. Brinkmann and M. H. Levitt, Symmetry principles in the nuclear magnetic resonance of spinning solids: Heteronuclear recoupling by generalized Hartmann–Hahn sequences, *J. Chem. Phys.* **115,** 357–384 (2001).

49. P. K. Madhu, X. Zhao, and M. H. Levitt, High-resolution ^{1}H NMR in the solid state using symmetry-based pulse sequences, *Chem. Phys. Lett.* **346,** 142–148 (2001).

50. M. H. Levitt, The signs of frequencies and phases in NMR, *J. Magn. Reson.* **126,** 164–182 (1997).

51. M. H. Levitt and O. G. Johannessen, The signs of frequencies and phases in NMR: The role of radio-frequency mixing, *J. Magn. Reson.* **142,** 190–194 (2000).

52. T. Gullion, D. B. Baker, and M. S. Conradi, New, compensated Carr–Purcell sequences, *J. Magn. Reson.* **89,** 479–484 (1990).

53. M. H. Levitt, Symmetry-based pulse sequences in magic-angle spinning solid-state NMR, *in* "Supplement to the Encyclopedia of Nuclear Magnetic Resonance" D. M. Grant and R. K. Harris (Eds.), Wiley, Chichester, England (1996), in press.

54. G. J. Boender, S. Vega, and H. J. M. de Groot, Quantized field description of rotor frequency-driven dipolar recoupling, *J. Chem. Phys.* **112,** 1096–1106 (2000).

55. M. H. Levitt, Composite pulses, *in* "Encyclopedia of Nuclear Magnetic Resonance" D. M. Grant and R. K. Harris (Eds.), Vol. 2, pp. 1396–1411, Wiley, Chichester, England (1996).

56. G. Metz, X. Wu, and S. O. Smith, Ramped-amplitude cross polarization in magic-angle-spinning NMR, *J. Magn. Reson. A* **110,** 219–227 (1994).

57. H. Geen, M. H. Levitt, and G. Bodenhausen, Preparing initial conditions for rotational resonance in solid-state NMR-spectroscopy, *Chem. Phys. Lett.* **200,** 350–356 (1992).

58. T. Karlsson, M. Edén, H. Luthman, and M. H. Levitt, Efficient double-quantum excitation in rotational resonance NMR, *J. Magn. Reson.* **145,** 95–107 (2000).

59. A. E. Bennett, C. M. Rienstra, M. Auger, K. V. Lakshmi, and R. G. Griffin, Heteronuclear decoupling in rotating solids, *J. Chem. Phys.* **103,** 6951–6958 (1995).

60. BioMagResBank (BMRB), Restricted set of amino acid chemical shifts, dated 12th February 2001, Department of Biochemistry, University of Wisconsin-Madison, http://www.bmrb.wisc.edu.

61. R. R. Ernst, G. Bodenhausen, and A. Wokaun, "Principles of Nuclear Magnetic Resonance in One and Two Dimensions," Clarendon Press, Oxford (1997).

62. E. Zaborowski, H. Zimmermann, and S. Vega, Distance measurements between ^{13}C nuclei in singly labeled p-xylene/dianin's inclusion compound by 2D-RFDR, *J. Magn. Reson.* **136,** 47–53 (1998).

63. A. E. Bennett, D. P. Weliky, and R. Tycko, Quantitative conformational measurements in solid state NMR by constant-time homonuclear dipolar recoupling, *J. Am. Chem. Soc.* **120,** 4897–4898 (1998).

64. S. R. Kiihne, K. B. Geahigan, N. A. Oyler, H. Zebroski, M. A. Mehta, and G. P. Drobny, Distance measurements in multiply labeled crystalline cytidines by dipolar recoupling solid state NMR, *J. Phys. Chem. A* **103,** 3890–3903 (1999).

65. Y. Ishii, J. J. Balbach, and R. Tycko, Measurement of dipole-coupled lineshapes in a many-spin system by constant-time two-dimensional solid state NMR with high-speed magic-angle spinning, *Chem. Phys.* **266,** 231–236 (2001).

66. M. L. Gilchrist, Jr., K. Monde, Y. Tomita, T. Iwashita, K. Nakanishi, and A. E. McDermott, Measurement of interfluorine distances in solids, *J. Magn. Reson.* **152,** 1–6 (2001).

67. N. C. Nielsen, F. Creuzet, R. G. Griffin, and M. H. Levitt, Enhanced double-quantum nuclear magnetic resonance in spinning solids at rotational resonance, *J. Chem. Phys.* **96,** 5668–5677 (1992).

68. T. Karlsson, C. E. Hughes, J. Schmedt auf der Günne, and M. H. Levitt, Double-quantum excitation in the NMR of spinning solids by pulse-assisted rotational resonance, *J. Magn. Reson.* **148,** 238–247 (2001).

69. C. Filip, X. Filip, M. Bertmer, D. E. Demco, and B. Blümich, Dipolar and J encoded DQ MAS spectra under rotational resonance, *J. Magn. Reson.* **150,** 184–193 (2001).

70. R. Tycko, A. T. Petkova, Y. Ishii, J. J. Balbach, N. A. Oyler, and O. N. Antzutkin, Structure of amyloid fibrils: NMR methods and results, *in* "2nd Alpine Conference on Solid-State NMR, Chamonix-Mont Blanc, France" (2001).

71. J. D. Gross, P. R. Costa, and R. G. Griffin, Tilted *n*-fold symmetric radio frequency pulse sequences: Applications to CSA and heteronuclear dipolar recoupling in homonuclear dipolar coupled spin networks, *J. Chem. Phys.* **108,** 7286–7293 (1998).

72. M. Hohwy, C. P. Jaroniec, B. Reif, C. M. Rienstra, and R. G. Griffin, Local structure and relaxation in solid-state NMR: Accurate measurement of amide N–H bond lengths and H–N–H bond angles, *J. Am. Chem. Soc.* **122,** 3218–3219 (2000).

73. B. Reif, M. Hohwy, C. P. Jaroniec, C. M. Rienstra, and R. G. Griffin, NH-NH vector correlation in peptides by solid-state NMR, *J. Magn. Reson.* **145,** 132–141 (2000).

74. J. C. C. Chan, C-REDOR: Rotational echo double resonance under very fast magic-angle spinning, *Chem. Phys. Lett.* **335,** 289–297 (2001).

75. J. C. C. Chan and H. Eckert, C-rotational echo double resonance: Heteronuclear dipolar recoupling with homonuclear dipolar decoupling, *J. Chem. Phys.* **115,** 6095–6105 (2001).

76. A. S. D. Heindrichs, H. Geen, C. Giordani, and J. J. Titman, Improved scalar shift correlation NMR spectroscopy in solids, *Chem. Phys. Lett.* **335,** 89–96 (2001).

77. E. H. Hardy, R. Verel, and B. H. Meier, Fast MAS total through-bond correlation spectroscopy, *J. Magn. Reson.* **148,** 459–464 (2001).

78. J. C. C. Chan and G. Brunklaus, R sequences for the scalar-coupling mediated homonuclear correlation spectroscopy under fast magic-angle spinning, *Chem. Phys. Lett.* **349,** 104–112 (2001).

79. V. B. Cheng, H. H. Suzukawa, and M. Wolfsberg, Investigations of a non-random numerical method for multidimensional integration, *J. Chem. Phys.* **59,** 3992–3999 (1973).

80. R. A. Haberkorn, R. E. Stark, H. van Willigen, and R. G. Griffin, Determination of bond distances and bond angles by solid-state nuclear magnetic resonance. ^{13}C and ^{14}N NMR study of glycine, *J. Am. Chem. Soc.* **103,** 2534–2539 (1981).

81. A. Naito, S. Ganapathy, K. Akasaka, and C. A. McDowell, Chemical shielding tensor and ^{13}C–^{14}N dipolar splitting in single crystals of L-alanine, *J. Chem. Phys.* **74,** 3190–3197 (1981).

82. M. S. Lehmann, T. F. Koetzle, and W. C. Hamilton, Precision neutron diffraction structure determination of protein and nucleic acid components. I. The crystal and molecular structure of the amino acid L-alanine, *J. Am. Chem. Soc.* **94,** 2657–2660 (1972).

83. V. F. Bystrov, Spin–spin coupling and the conformational states of peptide systems, *Prog. NMR Spectrosc.* **10,** 41–81 (1976).

84. A. Naito, S. Ganapathy, P. Raghunathan, and C. A. McDowell, Determination of the ^{14}N quadrupole coupling tensor and the ^{13}C chemical shielding tensors in a single crystal of *l*-serine monohydrate, *J. Chem. Phys.* **79,** 4173–4182 (1983).

85. M. N. Frey, M. S. Lehmann, T. F. Koetzle, and W. C. Hamilton, Precision neutron diffraction structure determination of protein and nucleic acid components. XI. Molecular configuration and hydrogen bonding of serine in the crystalline amino acids L-serine monohydrate and DL-serine, *Acta Crystallogr. Sect. B* **29,** 876–884 (1973).

86. M. Bak, J. T. Rasmussen, and N. C. Nielsen, SIMPSON, A general simulation program for solid-state NMR spectroscopy, *J. Magn. Reson.* **147,** 296–330 (2000).